The copyright of this thesis vests in the author. No quotation from it or information derived from it is to be published without full acknowledgement of the source. The thesis is to be used for private study or non-commercial research purposes only.

Published by the University of Cape Town (UCT) in terms of the non-exclusive license granted to UCT by the author.

University of Cape Town

University of Cape Town

Light induced degradation in hydrogenated amorphous silicon (a-Si:H).

Miss. Z. Sigcau

University of Cape Town

Thesis submitted to the faculty of science of the University of Cape Town in fulfilment of the requirements for the M.Sc. degree in Physics.

Abstract.

Light induced degradation in the microstructure and optical properties of a series of hydrogenated amorphous silicon (a-Si:H) layers, deposited by hot wire chemical vapour deposition system (HWCVD) on glass and silicon substrates at different temperatures ranging from 250°C to 500°C are investigated. Light soaking experiments were carried out using a mirrored chamber with a metal halide lamp. The radial distribution function (RDF) of the as-deposited samples showed an increase in the bond angle and a decrease in the radial distance indicating a relaxation of the amorphous network with increasing the deposition temperature T_d and illumination times. The changes in hydrogen bonding configuration whereby the total hydrogen content at different stages of illumination were compared and the monitoring of the bonded hydrogen content was via the transmission bands of the vibrational wag and stretching modes of the IR spectrum, and total hydrogen through the elastic recoil detection analysis (ERDA), respectively. Electron microscopies *i.e.* TEM and SEM were used to monitor the changes in the morphology and phase of the sample.

University of Cape Town

Table of Contents

Chapter 1

1.1 Introduction....1

1.2 Overview....3

Chapter 2

2.1 Structure of amorphous semiconductors....4

2.2 Structure of a-Si:H....5

2.3 Electronic properties....7

2.3.1 Electronic defect structure....8

2.3.2 The Staebler-Wronski Effect....9

2.4 Hydrogen migration....10

2.5 Oxygen structure....12

Chapter 3

3 Experimental techniques....14

3.1 Sample Growth Conditions....14

3.1.1 Background on HWCVD....15

3.1.2 Hot wire chemical vapour deposition technique....15

3.2 Radial distribution function. 17

3.3 Fourier Transforn Infared Spectroscopy....19

3.4 Electron Microscopy....23

3.4.1 Electron Diffraction.... .26

3.4.2 Structure of Electron Diffraction.... 27

3.5 Ultra-violet /Visible Spectroscopy (UV)....28

3.6 Ion Beam Analysis....29

University of Cape Town

Chapter 4

4 Experiments

4.1 Deposition Chamber....31

4.1 HWCVD chamber....32

4.1.1 Experimental....33

4.2 X-ray diffraction....34

4.3 Light soaking....37

4.4 FTIR Spectroscopy....39

4.5 Utraviolet / Visible Spectroscopy....41

4.6 Ion beam analysis....41

4.7 SEM....43

4.8 TEM....45

4.8.1 Experimental....46

Chapter 5.

5. Results.

5.1. Hydrogen
Content....48

5.1.1. Rutherford Back Scattering (RBS)....49

5.1.2 The FTIR and UV spectroscopy....50

5.1.3 The Bonding Structure....53

5.2 X-Ray diffraction....55

University of Cape Town

5.3 Scanning Electron Microscopy (SEM)..56
5.4 Transmission Electron Microscopy (TEM)..58

Chapter 6

6. Discussions...60
6.1 Hydrogen, Silicon and Oxygen bonding structures (FTIR spectra)....................60
6.1.1 Hydrogen content...60
6.1.2 Molecular Hydrogen H_2..61
6.1.3 Hydrogen Bonding Structure...63
6.1.4 Oxygen Bonding Structure...64
6.1.5 Band Gap...65

6.2 SEM measurements...67
6.3 Transmission Electron Microscopy TEM...68
6.4 X-ray diffraction...69
7. Conclusions... 71
References... .73

University of Cape Town

1.1 Introduction.

Hydrogenated amorphous silicon (a-Si:H) has been intensively investigated by several researchers over the past decades [1, 2, 3]. This interest can be attributed to its potential applications in commercial solar cell production, photovoltaics, and image devices such as sensors, electrophotography, and optical recordings [4, 5]. Even today it is still a material of choice for many researchers and is rapidly gaining commercial value in display technologies such as thin film transistors (TFTs) [6, 7], for use in active matrix liquid crystal displays (ANLCD), and as the active part in solar cell application [6, 7]. Disorder, caused by absence of long range order (LRO), the light induced *Metastability* known as Staebler-Wronski effect, and the presence of *atomic hydrogen* in the material are said to have a profound influence on the physical *i.e.* optical and electronic properties of a-Si:H [6, 7, 9].

The Staebler-Wronski effect is one of the major limiting factors for application of this material. In the past 27 years considerable amount of effort has been made on the understanding of this effect. But despite extensive experimental work and theoretical modelling, the origins of the effect are unclear. Over the last decade these theoretical models have been divided into two main classes of models: a) The first class is based on the idea of Si-Si or Si-H bonds: b) The second class is based on the formation creation of defects by the movement of a defect such as impurity, native defect, or H that is bonded in a special way [8, 9]. Within these classes there are competing models which includes; (a) Weak Si-Si bond breaking by non-radiative recombination [2, 5], and describes light induced degradation (LID) as a local effect

University of Cape Town

that involves *metastable* hydrogen; (b) The hydrogen collision model [4], which describes light induced degradation (LID) as long range hydrogen motion; (c) The relaxation of neighboring H-terminated dangling bonds [6, 7] to allow the recombination of molecular hydrogen as the diffusing species. Many more models are still being formulated.

In all the various models and theories, it has been suggested that hydrogen plays an active role, however it is still unclear how and what the role is. Also these models all lead to the same defect concentration dependence on illumination time and light intensity but with different efficiencies [5, 8].

In this project, I will report on the effect of the deposition temperature T_d and illumination time on the microstructure, optical properties and light induced degradation of a-Si:H layers grown by HW-CVD on glass and crystalline silicon (c-Si) substrates.

Chapter 2, deals with the theoretical background of a-Si:H, structural features such as defects and electronic properties are described, with special emphasis on their influence on the Staebler-Wronski effect and in addition the theory of the hydrogen migration and structure of oxygen impurity is discussed.

Chapters 3 and 4 are more concerned with the theoretical and experimental details of the instrumentation and the characterization techniques used, such as (i) electron microscopy *i.e.* transmission electron microscopy (TEM) and scanning electron microscopy (SEM). (ii) The deposition technique and the hot wire chemical vapor deposition (HWCVD) chamber. (iii) X-ray diffraction and the radial distribution

University of Cape Town

function (RDF). (iv) Ion beam analysis and Rutherford back scattering (RBS) and electron recoil detection analysis (ERDA). (v) Optical analysis and the Fourier infrared transform (FTIR) and ultraviolet/visible spectroscopy (UV-Vis) are all introduced.

In Chapter 5, I will show the effect of deposition temperature and light soaking in the ordering of the amorphous network which is characterized through the radial distribution function (RDF), derived from x-ray diffraction measurements. The changes in bonded hydrogen concentration C_H, are monitored by following the changes in hydrogen concentration of the isolated mono-hydride [Si-H], di-hydride $[Si\text{-}H]_n$ and poly-hydride $[Si\text{-}H_2]_n$ on the IR transmission spectra. The total hydrogen content C_H is calculated using elastic recoil detection analysis (ERDA) and then compared with bonded hydrogen concentration C_H. The amount of oxygen present in the network is calculated from the Rutherford backscattered spectroscopy.

From the optical measurements (UV) the effect of the deposition temperature T_d and illumination time on the band gap E_g are calculated and then compared. The electron microscopy (EM) techniques such as scanning electron microscopy (SEM) and transmission electron microscopy (TEM) are used to follow the change in the morphology and topography of the samples at different stages of illumination.

Chapter 6 deals with the discussion of the results, and chapter 7 concludes the work.

University of Cape Town

2 Structure and properties of amorphous semiconductors.

2.1 Structure of Amorphous Semiconductors.

The description of the structure of amorphous semiconductor is developed from the model proposed by Zachariasen in 1932 which describes the structure of this material as the 'continuous random network' (CRN) [2, 10, 11, and 12]. This is in contrast to crystalline semiconductors, whose structure is a periodic array of atoms as shown in Figure 2.1 (a), with the amorphous structure characterized by an irregular arrangement of atoms as shown in Figure 2.1(b).

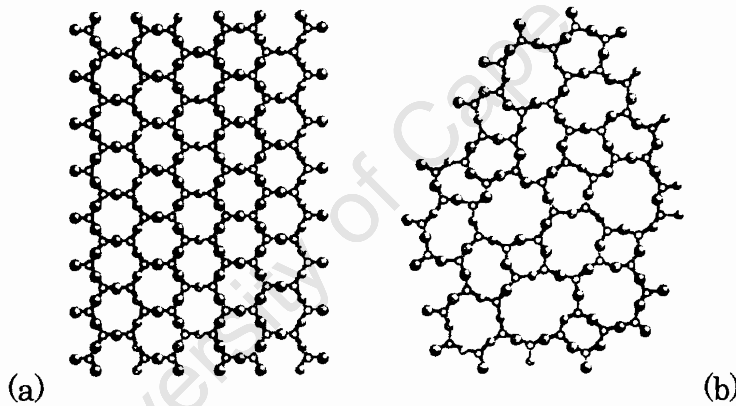

Figure 2.1(a) Structure of two dimensional oxide, (A_2O_3) in crystalline form,
(b) Amorphous form [13].

It has been confirmed by numerous experiments that the CRN model can successfully represent some major topological and other features of disordered tetrahedrally bonded materials [10, 13, 14], but the CRN is only an approximation, and the structure of the real material is much more complicated. The elementary defects found in amorphous semiconductors are the *coordination defects,* which occur when an atom has too few or too many bonds. This is in contrast to crystalline

University of Cape Town

materials where defects are vacancies, dislocations and interstitials [8, 11]. One of the features of amorphous semiconductors is that they are in a *metastable* state i.e. in a *non-equilibrium state.* This is brought on by different conditions during the formation process [15]. Amorphous semiconductors are characterized by the absence of *long-range order* (LRO), observed in crystalline semiconductors, with the *short range order* (SRO) the same as in crystalline silicon, and the *intermediate range order* (IRO) which might hold on a certain scale [8, 11, 14].

University of Cape Town

2.2 Structure of a-Si:H.

Both the SRO and IRO in the Si-Si network closely resemble the hydrogen free a-Si as seen in Figure 2.2. The nearest neighbour separation corresponds to the Si-Si covalent bond, and its value almost corresponds with that of crystalline silicon, $r_1 = 2.34$ Å, within 2 to 3 % fluctuation range and is independent of the amount of hydrogen in the sample [7, 8, 14].

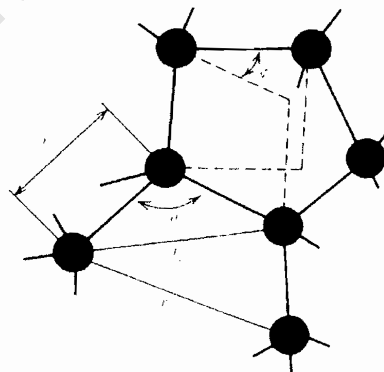

Figure 2.2 Three dimensional model describing the static structure of the disordered system where, r_1, r_2 and r_3 are the interatomic distance for the first, second and the third nearest neighbour, The statistical distribution of θ, r_1 and r_2 are used for indexing the SRO, while r_3 and φ are used for indexing LRO [14].

The bond angle θ ($\theta = 109,28^{o}$) shown in Figure 2.2 above and its distribution spread $\Delta\vartheta$ is nearly the same as that of a-Si but varies slightly depending on the preparation conditions. It is found to be nearly the same as that of a-Si from x-ray diffraction (XRD) results [8, 5, 12], but differences are observed in Raman scattering [16, 17, 18]. The coordination number r_1 decreases as the bonded hydrogen content C_H is increased. The defects in a-Si can take different forms, some are dangling bonds (three coordinate Si atoms) with energies near mid gap, and same are strained defects (normally 4-fold) sites with bond far from the tetrahedral angle. Floating coordinated bonds (5-fold) are also possible [11, 17, and 18].

2.3 Electronic Properties.

One of the fundamental electronic properties of an amorphous semiconductor is the presence of a band gap separating the valence band from the conduction band, which is explained by the splitting of the bonding and anti-bonding states of the covalent bond [7]. Theoretical studies have shown that the distortion of the bond length r and bond angle θ, originates from the structural long range disorder (LRO), and will result in the broadening of the tail states extending to the forbidden gap [7]. The electronic transport occurs at the band edge, hence the importance of band tails thus the width of the band not only depends on the degree of structural disorder, but also on the bonding character of the state [8].

There currently exist many models which describe the electrically important microscopic features within the amorphous network of pure a-Si < 1000 atoms, and

University of Cape Town

few for bulk a-Si:H. Most of those models are based on the following techniques *i.e* molecular dynamics (MD) [18, 20] employing empirical tight binding (TB) [21, 23] or pure quantum mechanical forces [22, 25]. All those models have been used to explain the important issues such as geometric nature of the paramagnetic defects [24], microscopic mechanism of light induced defect formation [26], and the nature of the band tail states [27].

Models of bulk a-Si:H though falls into two categories: i) static where atoms are arranged in a cell via predetermined geometric algorithms and then relaxed; ii) dynamic where atoms in an initial cell (c-Si) are annealed and then quenched.

2.3.1 Electronic defects in a-Si:H.

Dangling bonds are typical examples of defects in tetrahedrally-bonded amorphous semiconductors. In a-Si:H they occupy a position shown in Figure 2.3. Dangling bonds could be classified as neutral D^0, positive D^+, and negative D^- charge states, with densities ranging between 10^{15}- 10^{20} cm^{-3}, depending on the substrate temperature and other preparation conditions [8], and lead to electronically active defect state in the band gap E_g.

These arise from as a result of the band tail states, which are the result of bond angle distortion of tetrahedral bonded a-Si:H, (4-fold coordinated Si atoms).

University of Cape Town

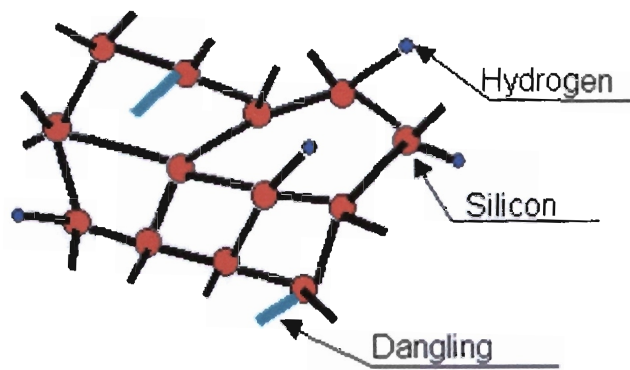

Figure 2.3 Two dimensional illustration of CRN containing atoms of silicon, hydrogen and a dangling bond at different coordination.

University of Cape Town

Hydrogenation of a-Si reduces the density of defects in gap states by passivating the dangling bonds, thus restoring the band gap, making a-Si:H applicable for solar cell devices [15, 28]. Even a small density of gap states can degrade the performance, and gap states are connected to degradation of device performance over time; hence understanding of the origin of its properties is crucial. The electronic state of dangling bonds is measured by electronic spin resonance (ESR) and electronic–nuclear double resonance (ENDOR) measurements [8].

2.3.2 The Staebler-Wronski Effect.

In 1977 Staebler and Wronski observed that a glow discharge deposited a-Si:H film illuminated for 2 hours at room temperature with strong light (≈ 200 m W/cm^2), suffered from reduced photoconductivity and dark conductivity, and that these properties are returned to their as-deposited values after annealing at temperatures above (160-200) °C [9, 15, 16]. Those changes were attributed to a reversible increase

of the density of gap states acting as recombination centers for photoexcited carriers, and leading to the shift of the dark Fermi level E_F towards the mid-gap [8, 22].

Exposure of device quality a-Si:H to light or excess carriers increases the density of neutral threefold coordinate dangling-bond (DB) defect by one to two orders of magnitude. Excess defects reduce carrier lifetimes and sharply limit the application of a-Si:H as an inexpensive solar cell.

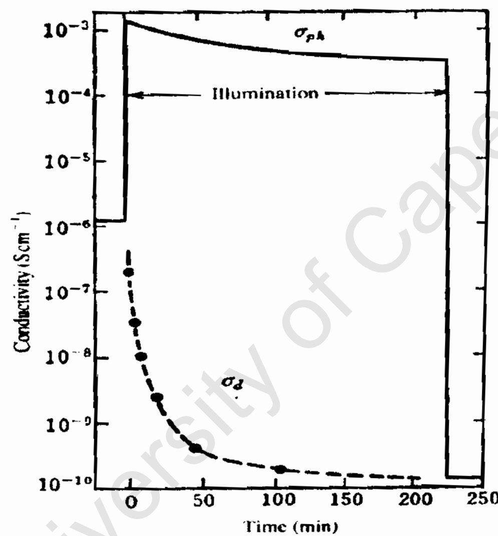

University of Cape Town

Figure 2.8 Photo and dark conductivity as a function of time before, during and after exposure to ~200mW/cm² of light at room temperature in the wavelength range 6000-9000Å. Substrate temperature during film deposition was ~300°C, film thickness was ~7000Å [9].

2.4 Hydrogen migration.

The silicon structure is said to be a rigid over coordinated network containing high strain energy, with negligible diffusion and has no apparent relaxation of the strain after growth. While the hydrogen structure is weakly bound and can diffuse within the material and across the surface and can partially penetrate the silicon network [8, 5].

In a-Si:H, the stable bonding configurations are Si-H bonds and unstrained Si-Si bonds which are too strongly bonded to the broken by hydrogen [7, 15, 29]. Highly strained Si-Si bonds (with energies close enough to the chemical potential of the hydrogen) are broken, and will either remain as Si-H bonds or will be reconstructed into singular Si-Si bonds. This leads to hydrogen scavenging the growth film of its weak strained bonds, resulting in a more ordered network. This ability for hydrogen to move in and out and within the sample is referred to as thermal diffusion D_H. Diffusion is explained as a multiple trapping model in which hydrogen is thermally activated from a distribution traps to an energy interstitial state [10, 13]. The time dependent diffusion coefficient is described by

$$D_H(t) = D_{oo}(\omega_o t)^{\beta-1} \tag{2.1}$$

$$D_H(t) = \frac{L^2}{4t} \tag{2.2}$$

where L is the diffusion length, and eliminating t we can express D_H as function of L.

$$D_H(L) = \left(\frac{4D_{oo}}{\omega_o L^2}\right)\frac{\omega_o}{4}L^2, \tag{2.3}$$

University of Cape Town

which describes diffusion in all the doped, and un-doped a-Si:H. The relaxation time τ then becomes

$$\tau = \frac{1}{D_H(L)}\left[\frac{4^{\beta-1}\beta a^2}{L^{2(\beta-1)}}\right] \tag{2.4}$$

2.5 Oxygen Bonding Structure.

Oxygen (O), nitrogen (N) and carbon (C) are some of the impurities found in a-Si:H, and the evidence of the effect of these impurities in solar-cell device performance has been observed [16]. These impurities have been found to significantly reduce the magnitude carrier diffusion length [12, 17] and enhance creation of metastable centers when the concentration of oxygen reaches levels in excess of 10^{20} cm^{-3}, or when nitrogen and oxygen reaches the levels of 10^{18} and 10^{17} cm^{-3} respectively [15, 29].

Oxygen is the most prevalent of all the unintentionally added impurities in a-Si:H, this is because of its high incorporation efficiency (1 ppm in gas phase results in 200 ppm incorporated in the film). From the results of secondary ion mass spectroscopy (SIM) oxygen levels were found to exceed 5 x 10^{15} cm^{-3} [29].

The incorporation of an oxygen atom into an a-Si:H structure may reduce the overall elastic energy of the solid. It also has been found to be a very efficient way of breaking and terminating dangling bonds, should annealing put oxygen in an approximate bridging position [29].

University of Cape Town

Incorporation of oxygen in the network may likely be due to an insufficient residual vacuum in the deposition chamber [31]. Oxygen can also be incorporated from the walls of the vacuum chamber in the form of H_2O, CO or CO_2 as contaminant of the SiH_2 source gas in the form of $(SiH_3)_2O$ and may occur upon exposure to air, at a rate which depends on the microstructure of the film [32, 33]. Various defects complexes contain oxygen *e.g* vacancy oxygen complexes, thermal donors, and oxygen precipitates which occur during the processing, and are of technological relevance. Oxygen might also be redistributed during light soaking when the Si-H bond is redistributed [9]. Kaiser et al. [34], Watkins and Corbett [8, 14] proposed models of oxygen in a-Si:H. In all these models, the oxygen atom occupies an interstitial position and is bonded to two silicon atoms as seen of Figure 2.7 below.

University of Cape Town

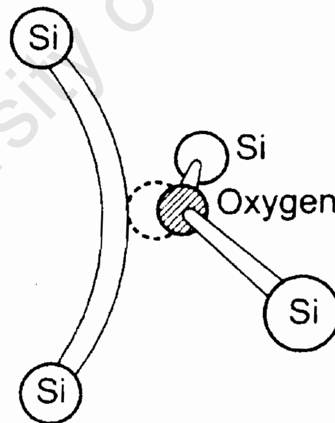

Figure 2.7 The model of a center vacancy-oxygen pair as derived from the paramagnetic resonance, vacancy site is dashed line, the open volume of the vacancy is strongly reduced by the interstitial oxygen [8].

3 Experimental techniques.

3.1 Sample Growth Conditions.

Amorphous semiconductors are prepared through non-equilibrium processes; hence properties of these materials depend on the method of preparation. The preparation conditions can be classified into three categories [2]. i) Rapid quenching from liquid phase. ii) Condensation from gas phase. iii) Formation from the solid. In this project we used the rapid condensation from gas phase.

Condensation from gas phase is an important reaction mechanism for many commercial uses and as far as our project is concerned we use the hot wire chemical vapour deposition technique HWCVD that is a technique that involves the rapid condensation following cracking of silane gas.

University of Cape Town

3.1.1 Background on HWCVD.

HWCVD was first reported by Wiesmann in 1979 as thermal CVD, but his results were not promising, due to the inferior electronic properties of the a-Si:H film compared to those deposited using plasma enhance chemical vapour deposition (PECVD) [1, 2]. It was not until 1985 when Matsumura and Tachibana first demonstrated a high-quality solar cell hydrofluorinated amorphous silicon (a-Si:F:H) using silicon di-fluoride (SiF_2) and hydrogen as gas precursors that researchers started to show an interest. In 1988 Doyle [36] grew high quality films using a slightly different technique to Matsumura and called the process "evaporated surface deposition" (ESD), later to be called HWCVD. Mahan *at al* [3] at the national

renewable energy labs (NREL) continued Doyle`s work and later did a comparable studies on a-Si deposited by ESD and by PECVD and found that HWCVD was superior, because of its low content of atomic hydrogen C_H and its reduced Staebler-Wronski effect [3].

3.1.2 Hot Wire Chemical Vapour Deposition technique (HWCVD).

Over the past decade this technique has emerged as the preferred deposition technique in the area of device fabrication, thin film transistors (TFT) with both a-Si and silicon Nitride (SiN_x) [9, 33]. Additionally, a-Si / poly-Si multi-band gap tandem solar cells (n-i-p / n-i-p structure) have been produced with thick absorbing i-layer with initial efficiencies of 8.1% and thickness of 1.1 μm. HWCVD is also used for the coating objects of complex shapes and nano-scale features and its conformal nature allows "shrink wrapping" of carbon nanotubes [37].

This technique has produced high quality and superior a-Si:H material compared to other deposition techniques. This is due to its higher deposition rates, at higher deposition temperatures (> 300°C), with low hydrogen concentrations < 1 at (%) [52], and the high growth rates achieved up to 10 (Å/s) at relatively low temperatures (~ 200°C) compared to other techniques such as molecular beam epitaxy (MBE) [8].

Hot wire chemical vapour deposition is the technique that involves the decomposition of precursor gases *e.g.* SiH_4, CH_4, NH_4 etc. on a heated filament, with

University of Cape Town

the constituent radical species often reacting in the gas phase and depositing onto a heated substrate as shown in Figure 3.1.

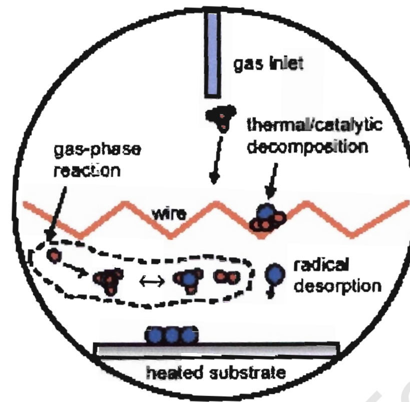

Figure 3.1 Schematic diagram of HWCVD, illustrating the various kinetic processes involved in the process [31].

The quality of the material deposited can be influenced by a number of reactor variables, which includes: the wire temperature, total pressure, gas flow rates, and the substrate temperature.

In HWCVD atomic Si produced by decomposition of silane on wire and SiH_3 produced by H abstraction on SiH_4 are believed to be the important radical species. These radicals are cracked at the surface of the hot filament (tungsten or tantalum) kept at a temperature higher than 1600 °C as shown in Figure 3.1. These species all have different gas phase and surface reactivities that can impact on film properties.

For example SiH_2 can readily insert into Si-H bonds [36], producing Si_2H_6 in the case of reaction with SiH_4. This species may dissociate, due to internal energy carried from reaction, or participate in further insertion reaction with SiH_2 provided that the pressure is high enough to stabilize the species. SiH_3 is unreactive with SiH_4

and is mostly likely to undergo recombination at high concentrations, briefly producing Si_2H_6 carrying larger amounts of internal energy before rapidly dissociating [32].

Atomic Si can also insert in Si-H bond of SiH_4, producing H_3SiSiH, which can isomerise to H_2SiSiH_2, provided dissociation does not take place [16]. Atomic Si and SiH are the most reactive species, with reaction probabilities near unity [38], while SiH_2 is near 0.6 [39] and SH_3 is between 0.1 and 0.4, depending on the hydrogen coverage of the surface [8].

3.2 Radial Distribution Function (RDF).

The presence of short range order (SRO) and the absence of long range order (LRO) in amorphous solids can be verified by diffraction studies extracted from the X-ray diffraction and neutron diffraction techniques [8, 13]. The scattered intensity from the X-ray is measured as the function of scattered angle γ, the structure factor $S(q)$ is measured as a function of wave vector q

$$q = (4\pi \sin \gamma)/\lambda \tag{3.1}$$

This is given by the radial distribution function J(r), which proportional to $r^2g(r)$ where g(r) is a pair distribution function resulting from the Fourier transformations of the diffraction measurements. If it is assumed that the substance is composed of one kind of atoms, the radial distribution function is given by:

$$J(r) = 4\pi r^2 \rho(r) = 4\pi r^2 \rho_0 + \frac{2r}{\pi}\int kf(k)\sin krdr \tag{3.2}$$

University of Cape Town

where $\rho(r)$ is the density of atoms at a distance r from the reference atom, ρ_o the average density of atoms, k the scattering vector

$$k = \frac{4\pi \sin\theta}{\lambda} \quad , \tag{3.3}$$

and $f(k)$ the reduced scattering intensity

$$f(k) = \frac{I(k)}{Nf^2} - 1 \tag{3.4}$$

where N is the number of atoms, f the atomic scattering factor and $I(k)$ the scattered intensity [7].

University of Cape Town

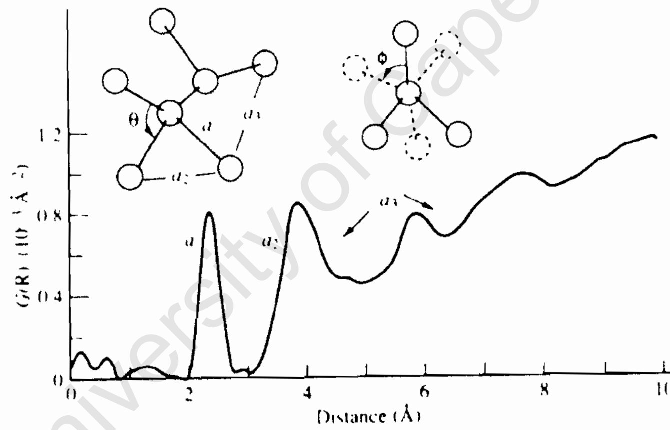

Figure 3.2 Schematic illustration of the structural origin of certain features in the density function for an amorphous solid with the narrow first peak and the broad second peak. The atomic spacing corresponds to the RDF as indicated. The atomic distance $a = r$ [13].

The area under f the first peak corresponds to the co-ordinate number 4 for c-Si and a-Si. The peak width is determined primarily by the thermal vibrations of the atoms and the type of instrumentation used. The second peak corresponds to interatomic distance for the second-nearest neighbours r_2, and is broadened and has a

shoulder in the case of a-Si, this indicates the variation of the bond angle $\theta \sim 10\%$, in r_2 the fluctuations increases significantly, thus showing loss of disorder [8]. The area corresponding to the second nearest neighbours r_2 will be the same as it is in the case of c-Si i.e. 12. The third peak of a-Si disappears (no long range order LRO).

3.3 Fourier Transform Infrared Spectroscopy.

Much of the information about the type of bond between silicon and hydrogen bonds is extracted from the vibrational modes and the wave length of the infrared absorption IR measurements. The IR absorption at frequency ω is proportional to the concentration of hydrogen as

$$N_H = f^2 A \int \left[\frac{\alpha(\omega)}{\omega} \right] d\omega \qquad (3.5)$$

where f is the local field factor, experience by the Si-H bond and A is a constant. From the IR spectra in Figure 3.3, the phonon modes occur in these energy bands:

Broad peak (transmission band) at 630 cm-1 associated with wagging mode, which describes wagging modes of vibration of mono-hydrides (Si-H) bonded species, as shown on Figures 3.3 and 3.4. The bonded hydrogen content C_H is determined by using this peak [7, 40].

$$C_H = A \int \frac{[\alpha(\omega)]}{\omega} d\omega \qquad (3.6)$$

where $\alpha\ (\omega)$ is the absorption coefficient at ω, and A is a constant of proportionality and is also inversely proportional to the cross section [40, 41].

University of Cape Town

A group of sharp peaks at (800- 900) cm^{-1}, describing the dihydride ($Si\text{-}H_2$) bonded species or poly-hydrides complexes $(Si\text{-}H_2)_n$ (isolated or clustered) Figure 3.3, with intensity depending on the deposition temperature T_d. Knight [40] suggested that in this vibrational band the voids and dangling bonds can readily be formed around the ($Si\text{-}H_2$) and $(Si\text{-}H_2)_n$ chains. C_H decreases as the deposition temperature T_d is raised and approaches zero at $T_d > 500$ °C [40].

A stretch mode at (2000- 2100) cm^{-1} describing vibration of mono-hydrides (Si-H) bonded species, and has a stronger stretching force compared to other vibrational bands.

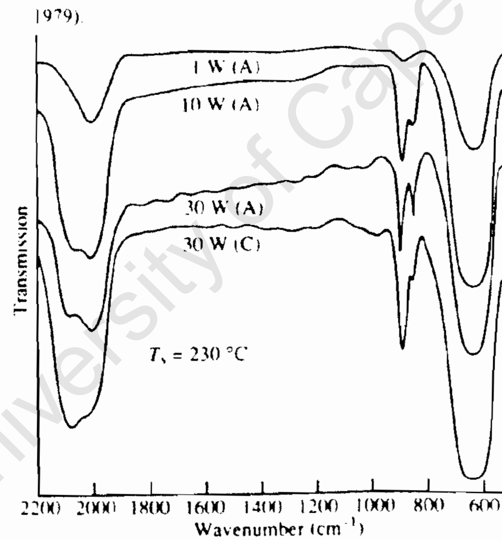

Figure 3.3 IR spectra for a-Si:H samples deposited at different growth conditions. The deposition power is indicated with (A) referring to anode and (C) cathode [8].

The other IR bands which are associated with impurities *i.e.* oxygen and nitrogen common in a-Si:H are located in: i) Oxygen related bands allocated at the wavelength of (500, 780, 980 and 2090) cm^{-1}.

University of Cape Town

The modes at 780, 980 and 2090 cm^{-1} are attributed to the vibration of the Si-O-Si-H group. The mode at 500 cm^{-1} is assigned to the out of plane rocking vibrational mode of the Si-O-Si group [30].

ii) Nitrogen vibrational modes are allocated at (495, 840 and 2060) cm^{-1}, the modes at 2060 cm^{-1} mode is caused by the shift of a-Si:H stretching mode associated with back bonded nitrogen. The mode at 840 cm^{-1} is associated with the Si-N stretching mode frequency. The 495 cm^{-1} vibrational mode associated with the bending mode of three Si atoms bonded to the nitrogen N [30].

University of Cape Town

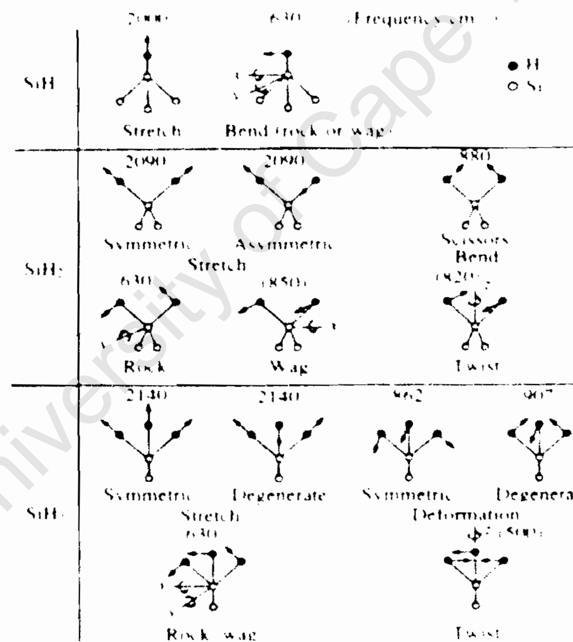

Figure 3.4 The set of Si-H vibrational modes for SiH, SiH_2 and SiH_3 groups, with calculated frequencies are shown [8].

From the above IR data and UV-Vis data we are able to obtain the optical parameters of amorphous semiconductors. These optical constants are strongly dependent on the process parameters and the interpretation of the optical

measurements requires a simple and reliable parameterization of the optical functions as a function of photon energy yielding film parameters such as thickness, surface roughness, dielectric functions, and optical parameters, hence the utilization of Tauc-Lorenz (TL) dispersion models which are traditionally used for disordered semiconductors [41].

University of Cape Town

3.4 Electron Microscopy.

Any electron microscopy of whatever type must have a source of high energy primary electrons, an Electron Gun. Its function is to produce a fine beam of electrons of precisely the same energy (*i.e.* velocity), all coming from the same source region [41, 42]. When a specimen is bombarded with electrons over a very small area, several things may happen to these electrons as shown in the Figure 3.5 below.

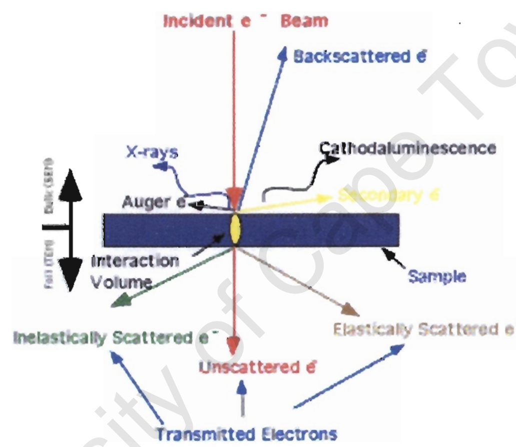

University of Cape Town

Figure 3.5 Signals generated when a high energy beam of electrons interacts with a thin specimen. Specimen interaction is what makes Electron Microscopy possible. The energetic electrons in the microscope strike the sample and various signals may be generated as shown above. Backscattered Electrons, Secondary electrons, Auger Electrons, X-rays, Unscattered Electrons, Elasticity Scattered electrons, Inelastically Scattered Electrons as shown above [42].

The reactions generated on the top side of the diagram are utilized when examining thick or bulk specimens with scanning electron microscopy (SEM) while the reactions on the bottom side are those examined in thin or foil specimens with transmission electron microscopy (TEM). The number of scattered events per unit

distance that the specimen travels through the specimen is *Q(t)*. If the specimen has thickness *t*, then the probability of scattering from the specimen is given by

$$Q(t) = \frac{N_o \sigma_T (\rho t)}{A} = P = \frac{1}{\lambda} \tag{3.7}$$

where ρ and t are called mass–thickness, N_0 is the Avogadro number and A is the atomic weight of the specimen [42]. The differential cross section $d\sigma/d\Omega$, describes the angular distribution of scattering when the electrons are scattered through an angle θ into a solid angle Ω.

University of Cape Town

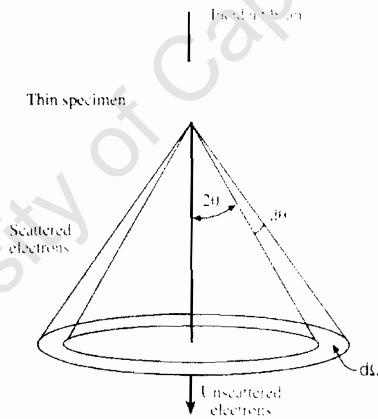

Figure 3.6 Electron scattering by a single isolated atom. The electrons are scattered through a semi angle θ and the total solid angle of scattering is Ω. An increase in the scattering angle dθ gives an increase in dΩ [43]

The differential cross section is given by

$$\sigma_\theta = \int_\theta^\pi d\sigma = 2\pi \int_\theta^\pi \frac{d\sigma}{d\Omega} \sin\theta d\theta . \tag{3.8}$$

Limits are governed by the fact that values of θ can vary from 0 to π, depending on the type of scattering. The atomic scattering factor is given by

$$|f(\theta)|^2 = \frac{d\sigma(\theta)}{d\Omega} \tag{3.9}$$

where $f(\theta)$ is the measure of the amplitude of an electron wave scattered from isolated atom.

$|f(\theta)|^2$ is proportional to the scattered intensity. The distance between two scattering events (mean free path length Λ) corresponds to the inverse of the total scattering cross-section Q_T:

$$\Lambda = \frac{1}{Q(t)} = \frac{A}{\left(N_o \sigma_T (\rho t)\right)} \tag{3.10}$$

$Q_T = N\sigma_T$ is a total scattering cross section where N is a number of atoms per unit volume, A is the atomic mass density, and N_o is Avogadro's number. The typical order of magnitude for Λ is 10 nm [42].

University of Cape Town

3.4.1 Electron Diffraction.

Electron diffraction can be described as a kinematic scattering process which occurs when an incident electron from an electron beam (typically 50-200 keV) with wavelength λ impinges perpendicular to a periodic row of atoms, with a regular interatomic spacing and meets the wave reinforcement and interference condition

given in the Bragg equation [16, 43]. The diffraction pattern contains basic types of information: (i) About the special arrangement which is given by the distance R between the central spot and other diffraction spot and rings, and the angle φ, between lines joining the central spot to each diffraction spot. (ii) Intensities in comparative values between the central spot and the diffraction maxima. (iii) The d – spacing, crystalline lattice parameter and the exact crystalline structure of the material if it is unknown.

3.4.2 Structure of Electron Diffraction.

The atomic arrangement plays a major part in electron diffraction.

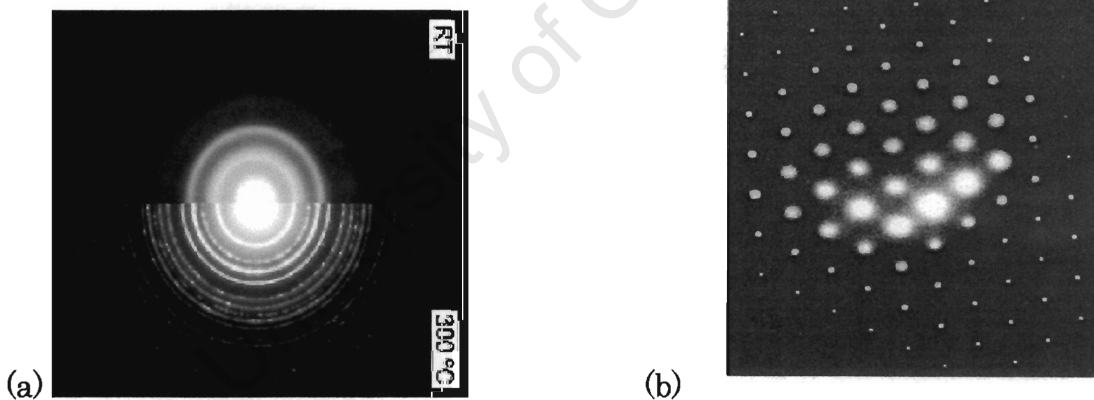

Figure 3.9 (a) Shows a sample which is amorphous before being illuminated at 300 °C, after illumination sample becomes poly-crystalline. (b) The single crystalline diffraction pattern.

In an amorphous structure the constituent atoms and molecules are arranged entirely randomly without any distinct repetition of the structure, then the diffraction patterns are very diffuse and contain little or no information that can be

analyzed quantitatively *i.e.* diffraction has a ring structure around a airy diffraction disc Figure 3.9 (a).

Figure 3.9 (b) shows diffraction for single crystalline specimen. The diffraction pattern is the record of the periodic structure and repetitive array of the atoms, made up of simple arrays of bright spots, which depend on the orientation of the crystal. Polycrystalline diffraction pattern Figure 3.9 (a) lower half consists of large number of small discrete areas, each with exactly the same atomic arrangement but at different orientation to each other. The single peaks of intensity occur in diffraction pattern, in the form of concentric rings [3, 44].

University of Cape Town

3.5 Ultra-violet /Visible Spectroscopy (UV- Vis).

This spectroscopy measure the amount of light transmitted or absorbed by a sample placed in the spectrometer. The wavelength at which a substance absorbs light is a function of its electronic structure. The intensity of the light absorption is related to the amount of the chemical between the light source and the detector, so a UV-Vis spectrum can be used to identify some chemical species [44].

In this project the correct UV-Vis spectra is crucial, since it help to predict the photoelectric behaviour of the device through optical parameters such as the refractive index $n(\lambda)$, the absorption coefficient $\alpha(\lambda)$. The Tauc–Lorenz plots are also extracted from the UV-Vis data .i.e. optical band gap E_g is also determined from the measurements [66].

Many UV-Vis spectrometers and visible spectrometers will give measurement values for transmittance *T*, absorbance *A* and reflectance *R* [7].

Absorbance is a measure of concentration of material present: negative log (base 10) of the Transmittance [- *log 1/T*], and can be expressed as product of extinction coefficient, path length, and concentration, written as in Beer`s Laws $AB = \varepsilon bc$.*i.e.* *A* is directly proportional to the path length *b*, and concentration *c* of the absorbed species [35].

3.6 Ion Beam Analysis (IBA).

IBA is used in element analysis and depth profiling of regions near surface (µm range) using Rutherford Backscattering Spectroscopy (RBS), Elastic Recoil Detection (ERD), and Nuclear Reaction Analysis (NRA) [5]. It is the spectral analysis of the secondary emission which leads to the detection of specific elements in the diverse samples as well as the determination of concentration of those elements.

Elastic Recoil Detection Analysis: is the primary technique of quantifying and depth profiling hydrogen in thin films, by measuring of recoiled ^{+}H and ^{2}H energies from an incident He ion beam, directed at a grazing angle onto a sample surface. The energy with which they are recoiled depends on the mass and on the recoil angle. From the measured energy spectrum of the recoils a concentration depth profile are calculated.

Rutherford Back Scattering: RBS provides absolute, quantitative depth profile of heavier elements in thin films. It is used to establish the compositions, film

University of Cape Town

thickness in multilayered structures, and accurately establish the homogeneous bulk composition. The incident ion is perpendicular to the sample surface. The measurement of the backscattered ^{+}He ions energies is based on the detection of the energy of charged particles, elastically scattered by the nuclei of the specimen. It allows the separation of the atoms masses of the elements and determination of the profile distribution as a function of the detected energy.

$$E = k(\theta, M_o, M_1) * E_o = \frac{M_o \cos\theta + [\sqrt{M_a^2 + M_o^2 \sin^2\theta}]^2}{[M_o + M_1]^2} * E_o. \qquad (3.11)$$

E_o are the atomic number and energy of the incident particle, and Z and E are the atomic number and energy of target nucleus respectively.

University of Cape Town

4 Experiments

4.1 Deposition Chamber.

The main part of every (HWCVD) deposition system is the vacuum chamber which is evacuated by a pumping unit to appropriate vacuum levels. Once the desired vacuum has been achieved, the process gas mixture is then introduced via Mass Flow Controllers (MFCs) and the pressure is kept constant by a variable conductance valve. The processed gas is decomposed at the hot filament (tantalum) by thermal catalytic reaction into radicals, as discussed in previous chapter 3 and Figure 4.1, and then deposited as thin films.

Each layer, and in particular the active semiconductor layer, must be deposited in high purity conditions in order to optimize its properties, that is the characteristics of the electronic devices.

The chamber used in this work is designed by the MVsystem Inc. in the U.S.A and is stationed at the University of the Western Cape.

University of Cape Town

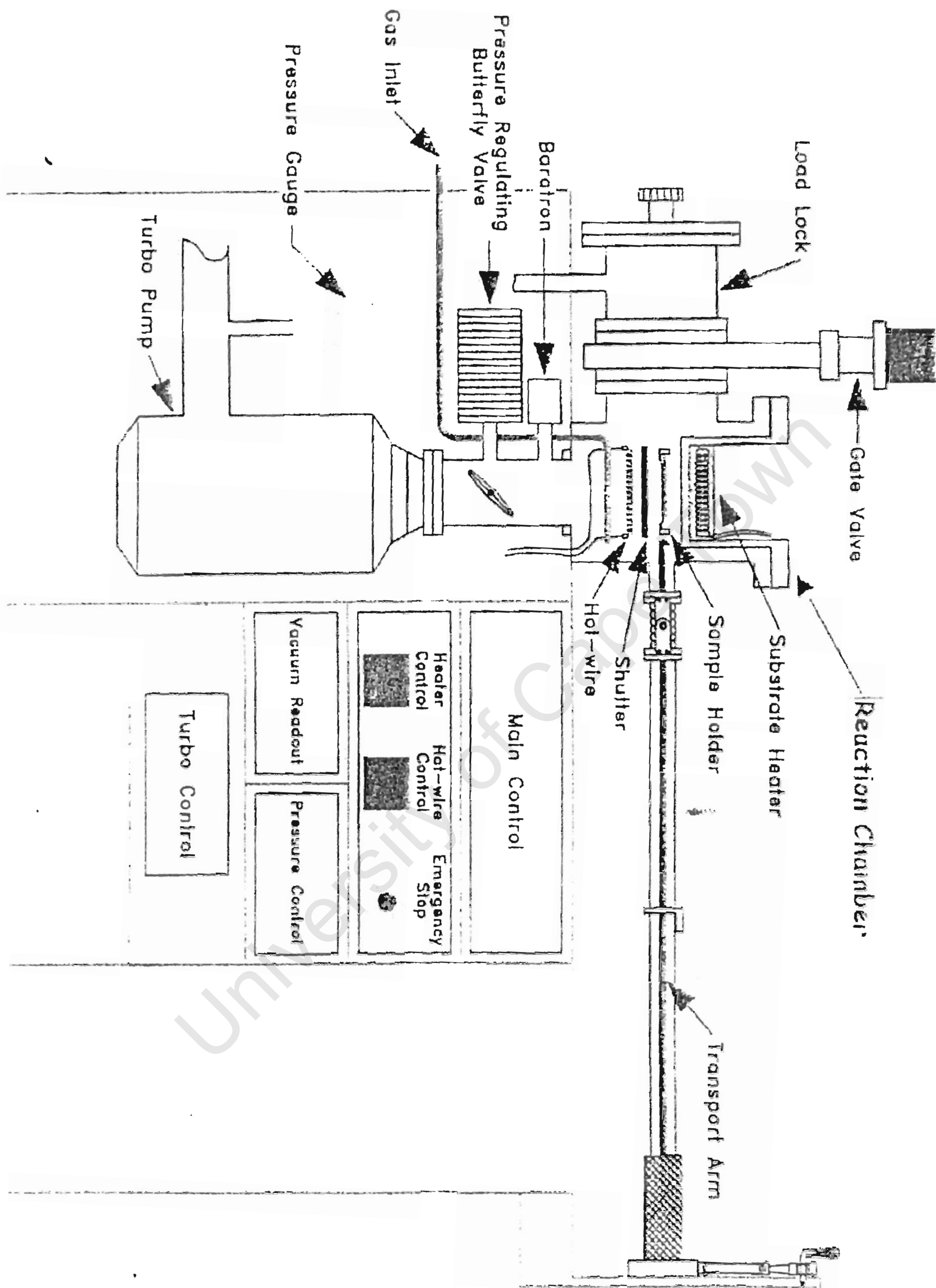

University of Cape Town

Figure 4.1 Schematic diagram of the HWCVD chamber with a coiled filament and three different gas inlet, showing , from top to the bottom : heater substrate : shutter top gas inlet .

4.1.1 Experimental details.

Thin films were deposited from a source gas of pure silane SiH_4 onto corning 7059 Borosilicate glass and single–crystalline silicon (100) substrates with no hydrogen dilution. Before every deposition the samples are first cleaned in methanol, then ultrasonically cleaned with ethanol and then the crystal silicon is soaked in 0.1% HF for about 5 min, the samples are then dried and placed in a 25x25 mm substrate holders. The samples are then placed in the load locked chamber, where they are then transported using the transport arm to the reaction chamber.

The reaction chamber Figure 4.1 consists of the substrate heater with seven parallel tantalum hot-wire filaments kept constant at 1600°C. The reactor is kept at a background pressure lower than $2x10^{-7}$ Torr.

For each deposition all the parameters are kept constant except the substrate temperatures which ranged from $250^oC - 450^oC$. The growth rate was controlled by the silane flow-rate which was kept constant at 60 sccm to obtain a film thickness ranging from 1.3 to 6 μm thickness (see Table 1 results).

After the deposition time (11 minutes) elapses the shutter is then closed and samples are brought back to the load lock chamber via the transport arm, and are then allowed to cool down in the chamber for approximately 1 to 4 hours depending on the deposition temperature T_d, so as to avoid oxidation. After the chamber has cooled down, the samples are then ready to be removed from the chamber.

University of Cape Town

4.2. X-Ray Diffraction.

X-ray diffraction was carried out in a (θ-2θ) goniometer from Bruker Analytical X-ray Systems (AXS) at iThemba LABS, operating at 40 kV and 40 mA in Bragg-Brentano geometry as shown on Figure 4.2 below. The x-rays are produced from an x-ray tube, and the source is $CuK\alpha$ radiation [43]. In any x-ray tube, x-rays are generated when a focused electron beam accelerated across a high voltage field bombards a solid target. As electrons collide with atoms in the target and slow down, a continuous spectrum of x-rays is emitted, which is termed Bremsstrahlung radiation.

University of Cape Town

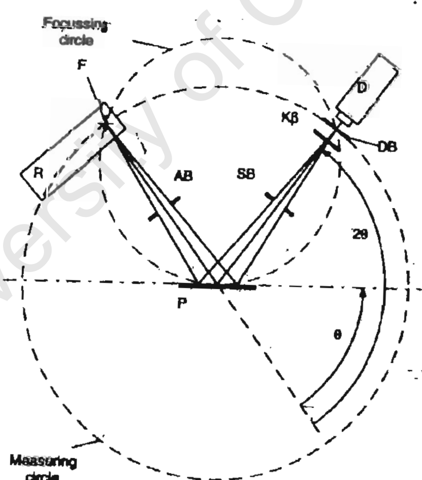

Figure 4.2 The x-ray beam path is shown; θ is the incident angle, 2θ is the diffraction angle, AB the divergence slits, D the detector, DB the detector slits, F the focus, $K\beta$ the filter, P the sample, R the x-ray tube and SB the antiscatter slit [43].

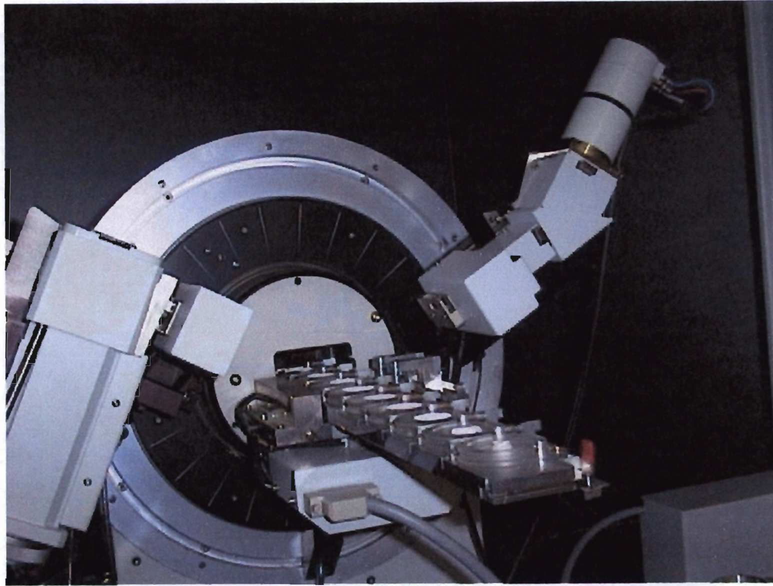

Figure 4.3 Bruker Analytical X-ray Systems (AXS) at iThemba LABS showing the X-ray tube housing with tube, Divergent slit, Goniometer, Detector, Monochrometer, antiscatter slits, sample holder.

University of Cape Town

The diffractometer is fitted with the following: i) the chiller which provides a source of clean water to cool the X-ray tube. ii) The regulator smoothes the generating current to provide a steady and dependable source of electricity to the diffractometer and its peripherals. iii) The computer sends commands to the diffractometer and records the output analysis. iv) The tube provides an X-ray source. Inside the tube there is a 40,000 V difference between a tungsten filament and copper target. The theta compensating slit collimates the x-rays before they reach the sample.

The sample chamber holds the specimen. The x-rays hit and scatter from the sample. The diffracted beams leave the chamber to the right where they can be detected by the scintillation counter which measures the x-ray intensity. Which is mounted on the goniometer (angle-measuring device). The goniometer is motorized and moves through a range of 2-theta angles. Because the scintillation counter is

connected to the goniometer we can measure the x-ray intensity at any angle to the specimen.

The diffraction patterns were recorded over a 2θ range from 10^0 to 68.72^0 with a step size of 0.04^0 with the diffraction time of 24 hours. The effects of the substrate and sample holder were subtracted from the raw signal by measuring the reverse side of the sample under identical conditions.

4.3 Light Soaking.

Light soaking experiments were performed using a mirrored chamber with an illuminance at the sample position of ~110Wm^{-2}. The chamber was built, with dimensions of 0.5 x 0.5 x 0.5 m^3, with the inside lined with mirrors. The outside of the box is made from supa-wood, which is relatively stable under temperature fluctuations (poor conductor). The sample holder stand is also made up of wood but is covered in reflective material (foil) [44].

Directly above the lamp a small part of the glass has been cut and fitted with an aluminium sheet to prevent the glass from breaking. This has been necessary because at the beginning we had a problem with the glass breaking (as the glass mirror heats up it expand, and when the light is then switched off the glass contracts and breaks). This has also been resolved by fitting an air-cooling system on the sides, which automatically switches on, on luminance but stays on after the light has been switch off.

University of Cape Town

The lamp of the light box is a metal halide lamp with a colour temperature of 5800 K (OSRAM HQI 400 W/D), and is mounted horizontally on the back of the mirrored box; 40 cm from the bottom mirror and 10 cm from the top mirror Figure 4.4.

Figure 4.4 The light box lined with mirrors; Halide lamp, sample stand, and the forced air cooling at the door and on the top sides of the box.

The use of this mirror box increases the luminance by a factor of 20, compared to the naked bulb at the same distance (40 cm). Before the actual experiment the conditions of the box (inside) are investigated as follows; an electronic thermometer and a light meter were placed inside the box under operational conditions to measure the environment at the sample position. The temperature was found to stabilize at 30 $\pm$ 1 ^{o}C and the intensity of 75 $\pm$ 5 x 10^3 Lux within 20 minutes.

4.4 Fourier Transform Infrared Spectroscopy (FTIR).

The main advantage of FTIR is a high spectral resolution, good signal to noise ratio, and its ability to measure a broad spectrum (400-10 000) cm^{-1} in relatively short amount of time [16, 47]. The fundamental component of the FTIR is a Michelson Interferometer, Figure 4.5.

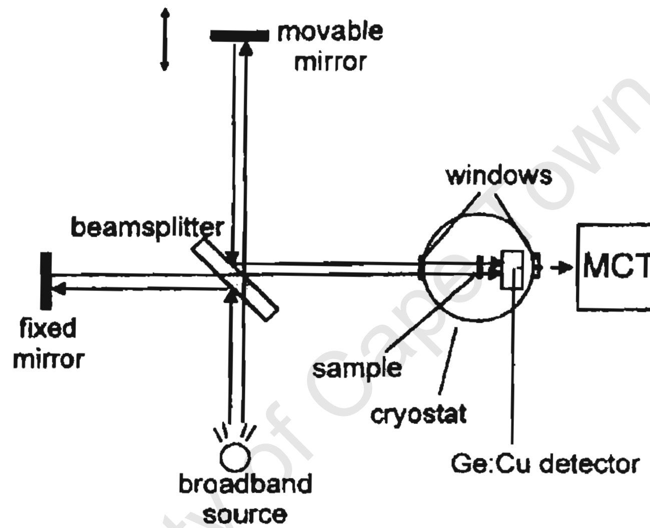

Figure 4.5 Schematic diagram of the spectrometer of the FTIR The beam splitter and the two mirrors comprise the interferometer [31].

University of Cape Town

The initial spectrum taken by FTIR is called an interferogram, it gives the beam intensity as a function of mirror position, $I(\delta/2)$ [8,17]. Fourier transform of interferogram is given by

$$I(\sigma)=\frac{2}{c}\int I\left(\frac{\delta}{2}\right)\cos\left[2\pi\sigma\overline{Z}\right]dZ \qquad (4.1)$$

where $\delta/2$ is the position of the movable mirror, Z is the difference in optical length of the optical path length of the two waves, $I(\sigma)$ is the intensity as a function of the wavenumber where $\sigma = (1/\lambda) = (v/c)$ and C is a constant.

FTIR transmission spectra as function of the vibrational wave number were collected on layers deposited on crystalline substrates (c-Si) using a Perkin-Elmer spectrum one in the energy range 400 - 4000 cm^{-1} with a resolution of 4 cm^{-1}, as shown in the Figure 4.6 below.

of Cape Town

Figure 4.6 Photograph of showing the Perkin-Elmer spectrum one, FTIR spectrometer.

4.5 UV -Visible spectroscopy.

The UV-Vis is taken from the absorption measurements of the layers grown on glass substrate. The absorbance spectrum Abs (σ) is given by

$$Abs(\sigma) = -\log_{10} \frac{I_B(\sigma)}{I(\sigma)} \quad . \tag{4.2}$$

For the UV-Vis measurements a Cary/1E/ UV-Vis spectrophotometer with monochromatic light in the energy range 1.2 to 2.4 eV with an energy resolution of 30 meV was used. The sample is put horizontally into the sample holder and placed inside the spectrometer chamber. The chamber is then closed and the veil placed on top of the chamber to shield light from coming through. The background is then taken, after that the samples is then measured using the Carry OPTICS (TM).

The optical parameters were determined from the reflection measurements of the layers grown on glass substrates. The thickness of the samples were estimated by computer analysis from the interference fringes of transmission spectrum to an accuracy of better than 1% using the correction proposed by Swanepoel [75], since our samples had thickness greater than 1 micron.

University of Cape Town

4.6 Ion Beam Analysis.

It is the spectral analysis of the secondary emission, which leads to the detection of specific elements in the diverse samples as well as the determination of concentration of those elements. Ion beam analysis (IBA) is used in element analysis and depth profiling of regions near surface (μm range) using Rutherford backscattering spectroscopy (RBS), elastic recoil detection analysis (ERDA) and nuclear reaction analysis (NRA).

University of Cape Town

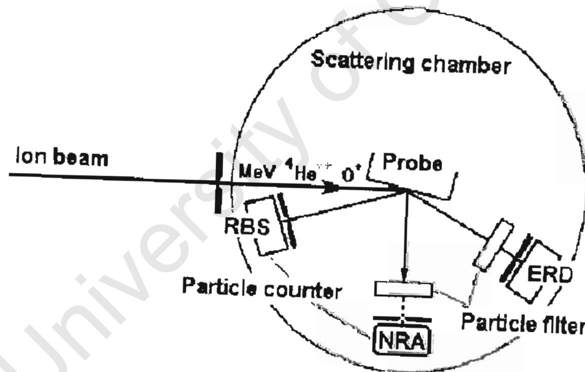

Figure.4.7 Schematic representation of an ion beam experiment, emitting different kinds of signals which are detected by detectors.

The ion beam analysis techniques *i.e.* Rutherford backscattering (RBS), elastic recoiled detection (ERDA) were performed at iThemba Labs using a 5.5 MeV Van de Graaff accelerator, that produces an accelerated beam of helium ion in the energy interval of 3.00 to 3.75 Mev (RBS) and 3.00 Mev (ERDA). For RBS / Resonance

scattering setup, the sample were tilted at an angle of 10° with respect to the incident beam. A solid surface barrier detector (100 mm^3 detection solid angle 1.15 msr) was placed at a laboratory scattering angle of 165° and for the ERD the samples were at 75° to the incident beam and the detector was at a scattering angle of 30° (all measurement were done separately). The filter with the detector was mylar of 12.5 μm thickness.

4.7 Scanning Electron Microscopy (SEM).

In a scanning electron microscope, a tiny electron beam is scanned across the sample. Simultaneously, the generated signals are being recorded, and an image is formed pixel by pixel. In SEM, the signals are observed on the same specimen site as the incoming electron beam using transmitted electrons. In contrast to TEM methods which require very thin samples, compact samples can thus be investigated by SEM. Valuable information about morphology, surface topology and composition can be obtained.

The UCT microscope (Figure 4.8) is capable of a resolution of 3 nm at 40kV with a LaB_6 filament and is controlled by computer and the images produced are digital. This enables experiments to be automated and enables the images to be analysed directly. The digital images can also be stored on magnetic disc and can be output on a variety of different media including 35 mm colour film, 120 monochrome film and A4 video print. It is also possible to record the session on videotape (VHS or S-VHS).

University of Cape Town

The detector used was the secondary electron (SE) detector. The design of the secondary electron detector enables specimens to be examined horizontally, thus overcoming the geometric distortions introduced by viewing tilted specimens. Signals from any two of the secondary electron (SE) detector, single channel analyzer (SCA), back scattered (BS) detector or Cathodoluminescence (CL) detector can be viewed simultaneously. An infrared video camera enables the inside of the chamber to be monitored continuously.

University of Cape Town

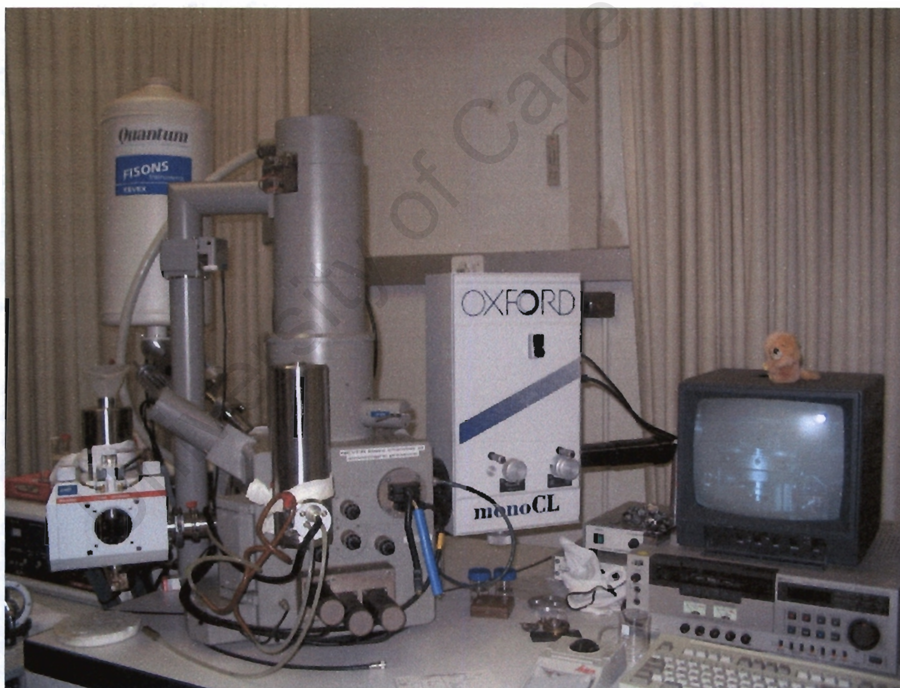

Figure 4.8 Photograph showing the SEM system; comprises of the Leica S440 digital scanning electron microscope and three major subsystems - The Fisons Kevex Energy, Dispersive X-Ray Analysis System, The Fisons LT7400 Cryo Transfer System and the Oxford Monochromator Cathodoluminescent system.

4.8 Transmission electron microscopy (TEM).

In the TEM an electron gun is used to focus a small, thin, coherent beam by the use of condenser lenses (see Figure 4.9). The first lens (usually controlled by the spot size knob) largely determines the spot size and the general size range of the final spot that strikes the sample. The second lens (usually controlled by the intensity or brightness knob actually changes the size of the spot on the sample; changing it from a wide dispersed spot to a pinpoint beam.

When a beam strikes the specimen parts of it are transmitted, this transmitted portion is focused by the objective lens into an image. The image is passed down the column through the intermediate and projector lenses, being enlarged all the way.

When the image strikes the phosphor image screen, light is generated, allowing the user to see the image. The darker areas of the image represent those areas of the sample where fewer electrons were transmitted through (they are thicker or denser). The lighter areas of the image represent those areas of the sample where more electrons were transmitted through (they are thinner or less dense) [43].

University of Cape Town

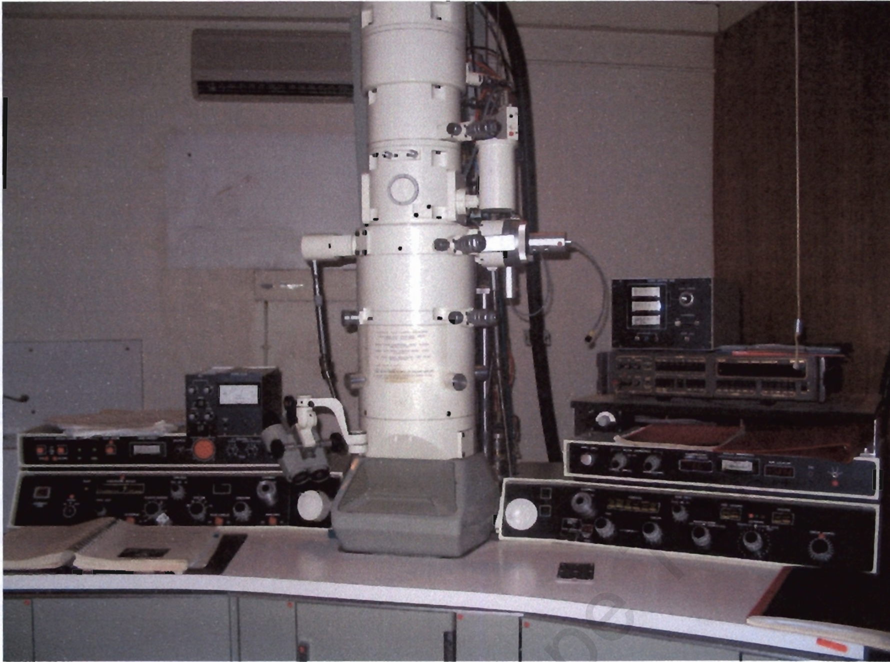

Figure 4.9 The EM -2000CX electron microscope operating at 200 kV for both TEM and ED measurements.

University of Cape

4.8.1. Experimental.

We scraped the films from the glass substrate and directly placed the fragments on a carbon-coated TEM grid. The drawback of this technique is that fracture along the growth direction cannot be controlled. As a consequence, in-homogeneities on the sample surface may be harder to observe than from other conventional preparation techniques. The grids were examined in an electron microscope (EM -2000CX) Figure 4.9 operated at an accelerating voltage of 200 kV.

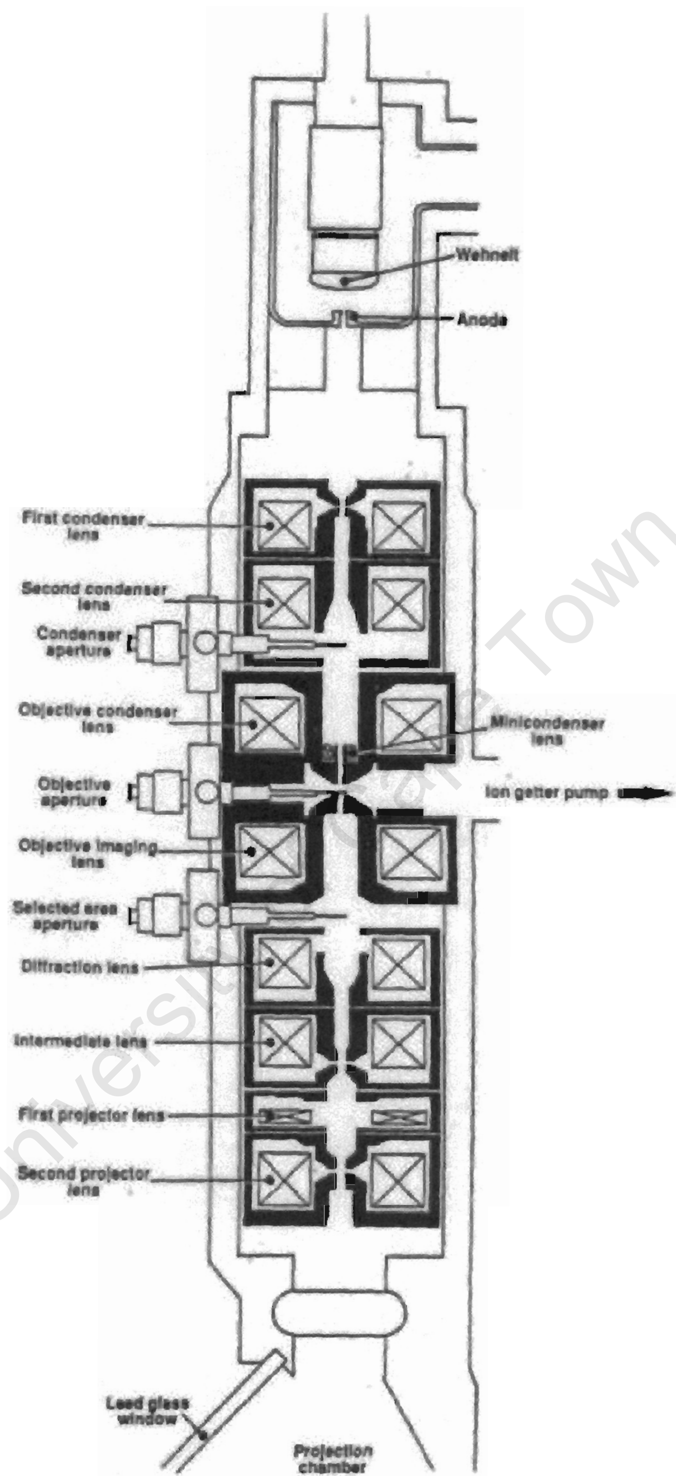

Figure 4.10 TEM microscope showing the components involved in image formation.

5. Results.

5.1 Hydrogen Content

Table 1 shows the summary of the hydrogen content and characteristics of all the samples, which were obtained as described in chapter 4. All the deposition parameters were kept constant *i.e.* pressure at 40 µbar, silane SiH_4 flow rate at 60 sccm, deposition time at 11 minutes except for Mw 141 which was deposited for 20 minutes.

Sample ID	Substrate T (oC)	*Thickness (nm)*	H content (%) FTIR/UV	H content ERDA (.%)	4hrs ERDA (%)	8hrs ERDA (%)	Absp.Coef ($10^4 cm^{-1}$)	Band gap (eV) as deposited
Mw153	450	1320	5.2	9.8	8.0	5.5	2.81	1.70
Mw141	400	3900	-	9.9	-	6.0	1.33	1.67
Mw152	350	1550	7.7	10.8	8.5	6.0	2.33	1.73
Mw145	250	2800	11.6	Irreg. dist. of H	Irreg. dist ofH	Irreg. dist ofH	1.38	1.82

Table 1.

Table 1. Shows how the growth rate, sample thickness, hydrogen content from both the FTIR and ERDA, absorption coefficient and the band gap are related to both the deposition tempretures and illumination times.

The thickness, growth rate, bonded hydrogen C_H, band gap E_g,, and total hydrogen content decreases with both the growth temperature and illumination time, while the and the absorption coefficient increase with growth temperature.

University of Cape Town

5.1.1 Elastic recoil detection analysis (ERDA).

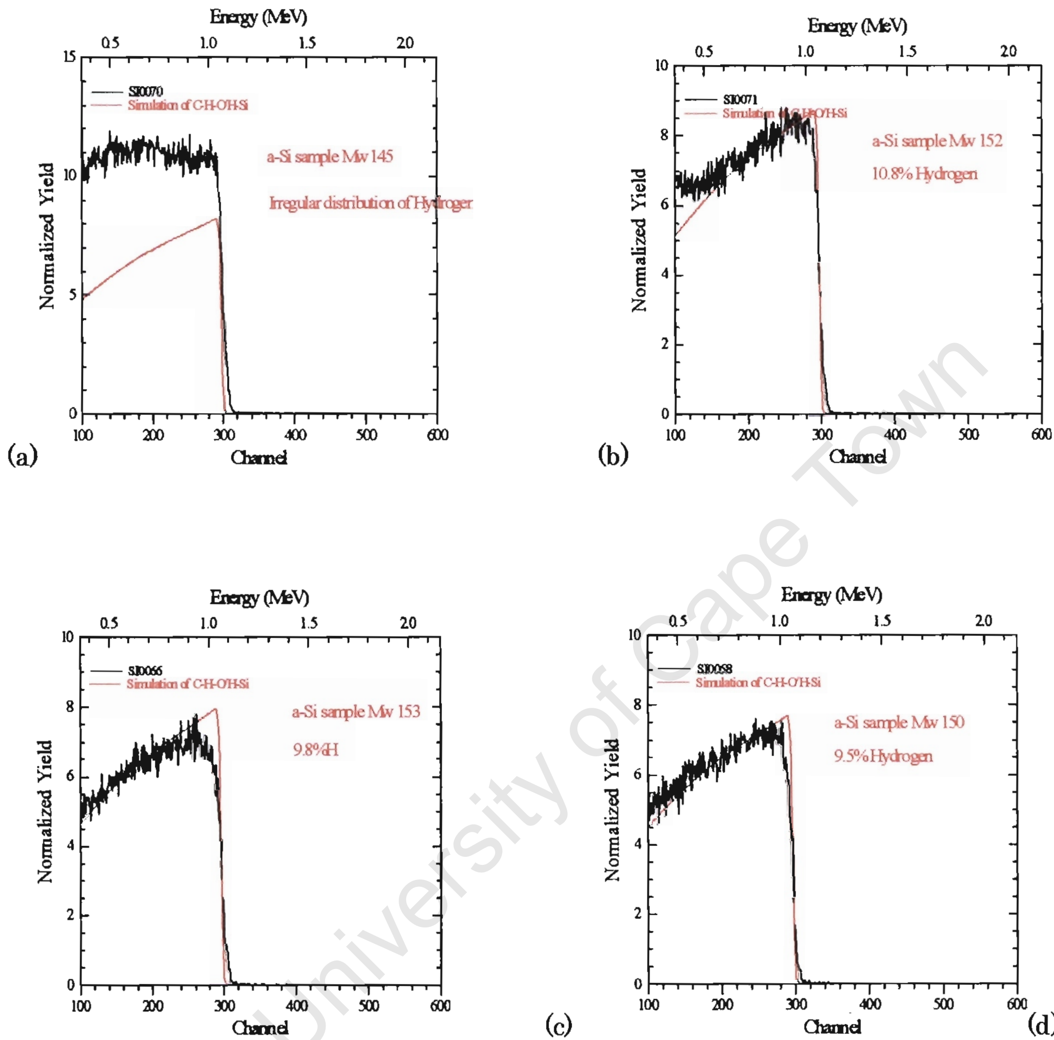

Figure 5.1 ERDA data for different deposition temperatures T_d at (a) 250°C, (b) 350°C, (c) 450°C and (d) at 400°C.

University of Cape Town

The total hydrogen content is extracted from the ERDA curves, using the RUMP program. The red line is a model estimate of the hydrogen. For Mw 145 there is an irregular distribution hence we can not simulate the H content.

5.1.2 FTIR and UV-Visible spectroscopy.

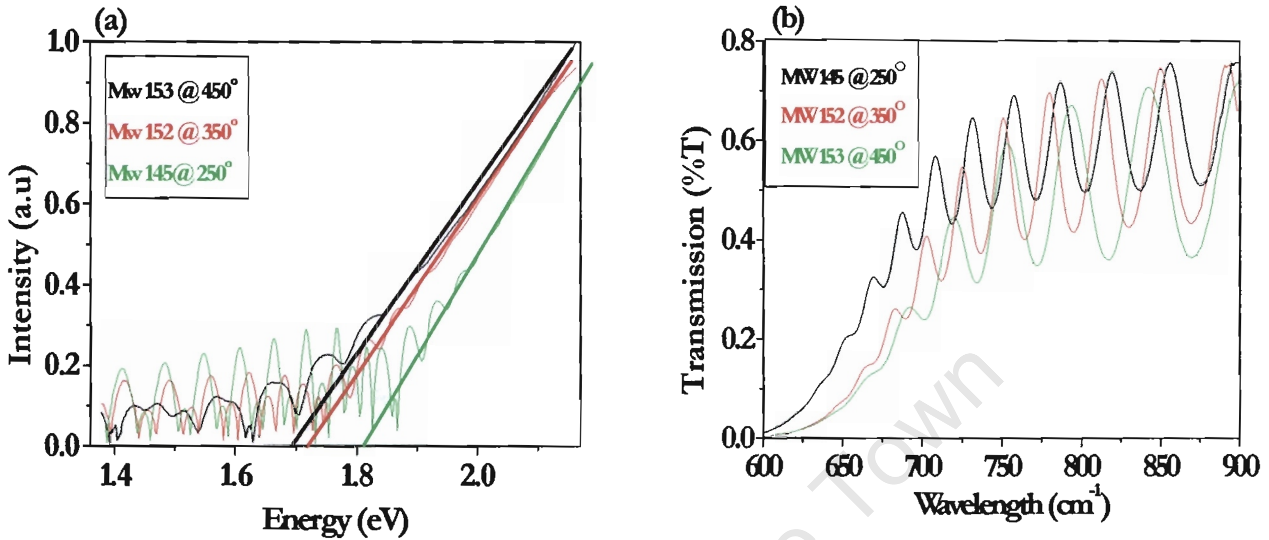

Figure 5.2 (a) Tauc plots against energy *hv* (eV). (b) The transmission (*%T*) extracted from the UV against wavelength (cm^{-1}).

Figure 5.2 (a) shows the Tauc plots from which the variation of the band gap E_g (green, red and black lines) is extracted. The higher the growth temperature, the lower the band gap E_g, Figure 5.2 (a). Figure 5.2 (b) shows how the growth temperature affects the absorption, the lower the growth temperature the higher the absorption, see black line. For higher deposition temperatures, green line has less absorption peaks. The thickness of the film is extracted from the interference peaks of the absorption curves Figure 5.2 (b) (black, green and red).

University of Cape Town

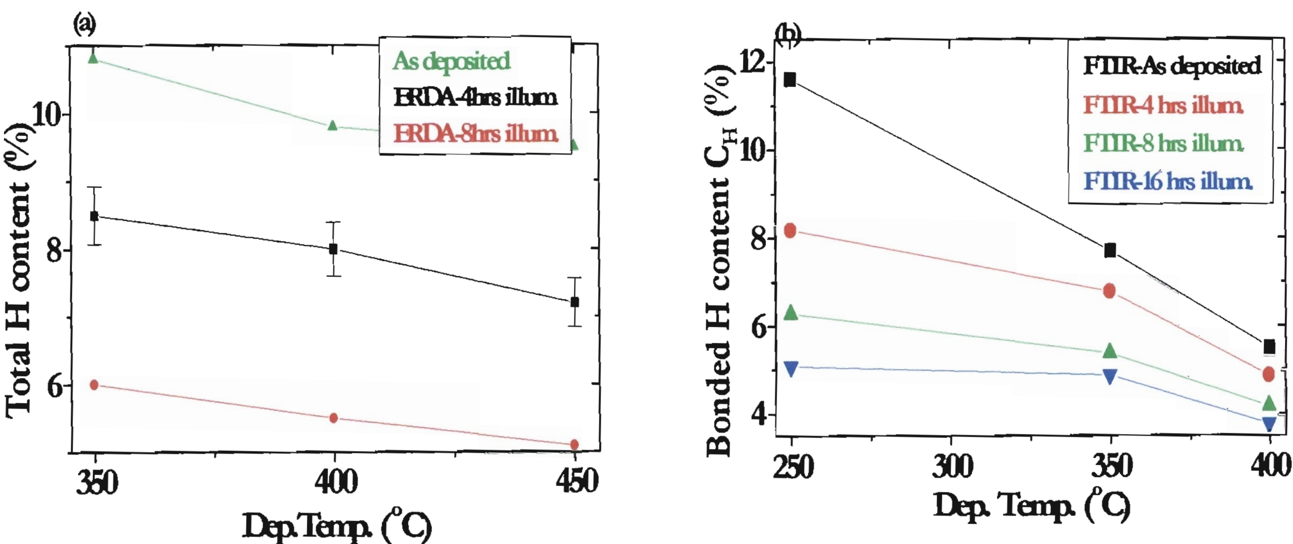

Figure 5.3 (a) shows the variation of the total hydrogen content from the (ERDA) spectra, (b) the bonded hydrogen content extracted from the wag mode of the IR spectra as a function of both the deposition temperature and illumination time.

The total hydrogen content from ERDA shown in Figure 5.3 (a), decreases with deposition temperature as seen from the green line, after illumination the same trend is seen blacklines after 4hours and red lines after 8hours. Figure 5.3 (b). A similar decrease is observed for the bonded hydrogen after the sample has been illuminated for 4 (red line), 8 (green line) and 16 (blue line) hours and against deposition temperatures

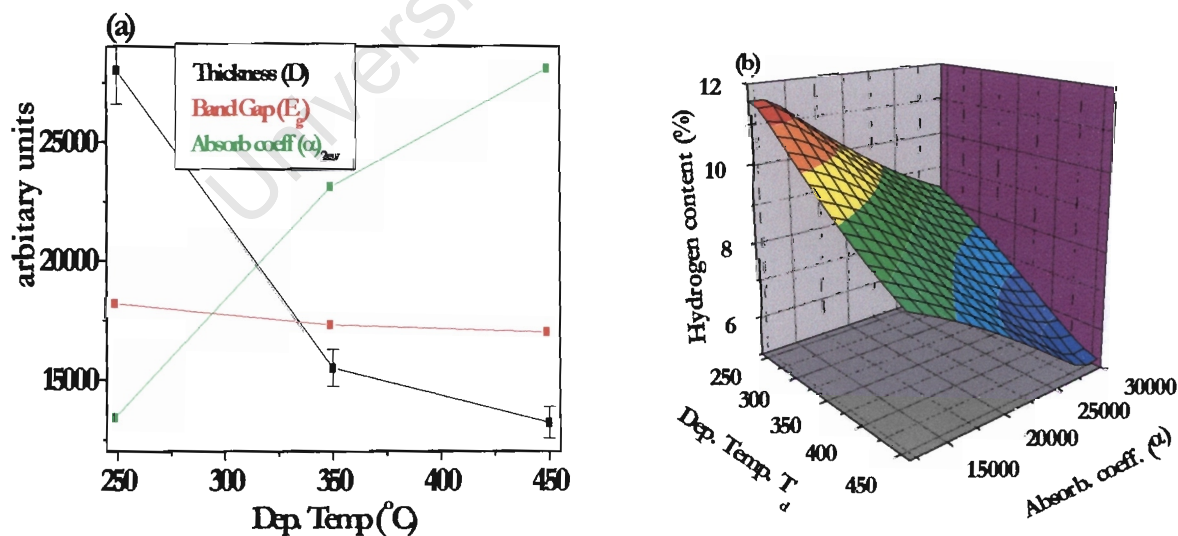

Figure 5.4 (a) The band gap E_g, thickness d (nm) and absorption coefficient (α_{2ev}) Vs T_d.
(b) 3-D showing the variations of deposition temperature with and the hydrogen content C_H and band gap E_g and with absorption coefficient.

University of Cape Town

In Figure 5.4, the thickness (black line) and the band gap (red line) decrease whereas there is an increase in absorption coefficient (green line) with growth temperature.

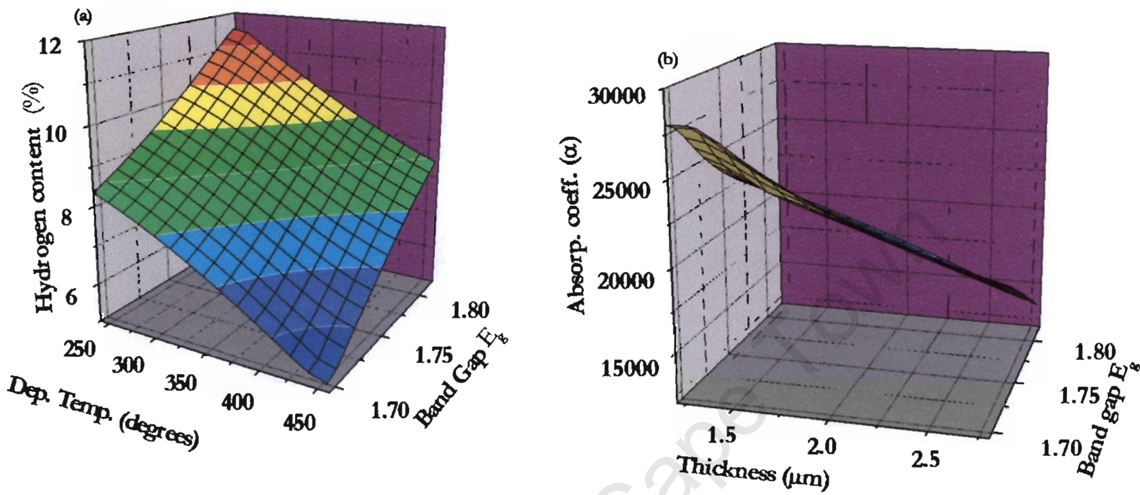

Figure 5.5 (a) Shows the variations of the deposition temperature with the hydrogen content C_H and the band gap E_g. (b) Shows the variation with absorption coefficient.

Figure 5.5 shows a three dimensional graphs of the thickness (d), optical band gap E_g, hydrogen content C_H and absorption coefficient (α_{2ev}). The optical band gap E_g increases linearly with increasing hydrogen content C_H and decreases with the increase in deposition temperature T_d and absorption coefficient (α_{2ev}).

University of Cape Town

5.1.3 The Bonding Structure.

Sample	*Dep.Temp*	*Si-H wagg 640*	*Si-H2/Si-Hn 800-900*	*Int.O 100-1200*	*1200-1300*	*2000-2100 Si-H/Si-H2*	*2500-2300 CHn*	*3500-3700*
Mw145	*250*	*651*	*853/895*	*None*	*None*	*2104*	*2926/2848*	*None*
Mw152	*350*	*643*	*890*	*None*	*None*	*2004/2105*	*2925/2848*	*None*
Mw153	*400*	*630*	*none*	*None*	*None*	*2002*	*2925/2848*	*None*

Table 2.

.

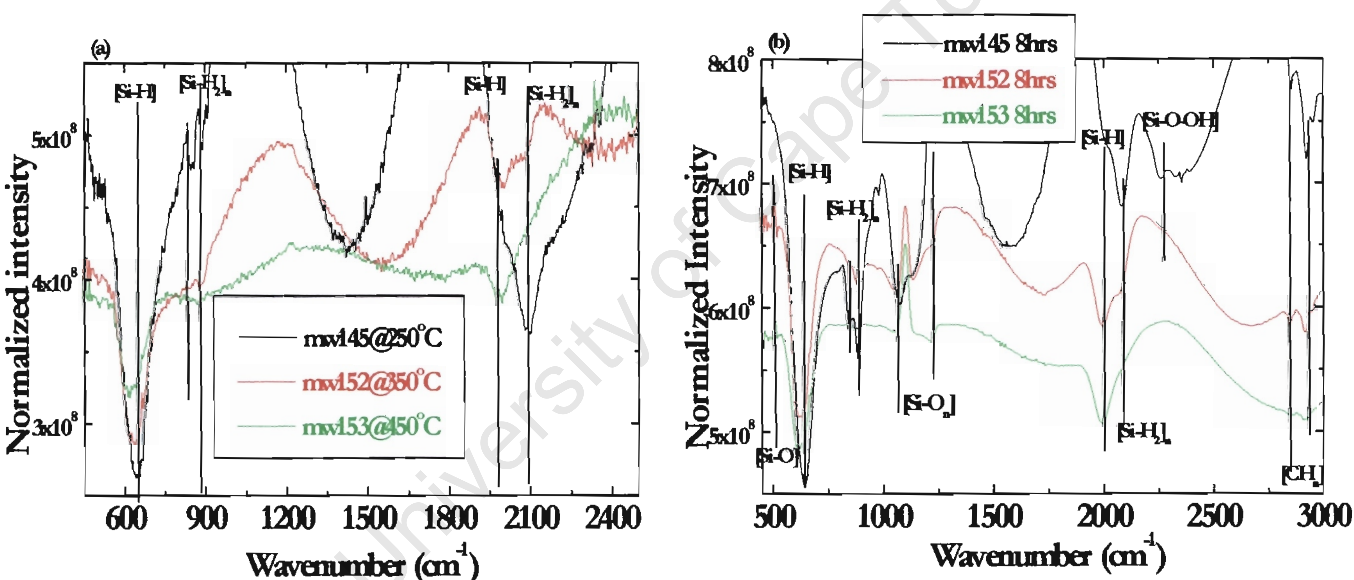

University of Cape Town

Figure 5.6 (a) shows the FTIR spectra against the wavelength, for as deposited (b) Shows the IR Spectra after eight hours of illumination.

From Table 2 and Figure 5.6 (a) for higher growth temperatures the mono-hydrides are the dominant bonding species (Mw 153 green line) at 2000 cm^{-1}. While for lower growth temperatures poly and di-hydrides are dominant (black Mw 145 and red line Mw 152) at 2100 cm^{-1}.from figure 5.6 (b) illumination times follow the same trend as growth temperatures, with vibrational modes of the film tending towards the mono-hydrides.

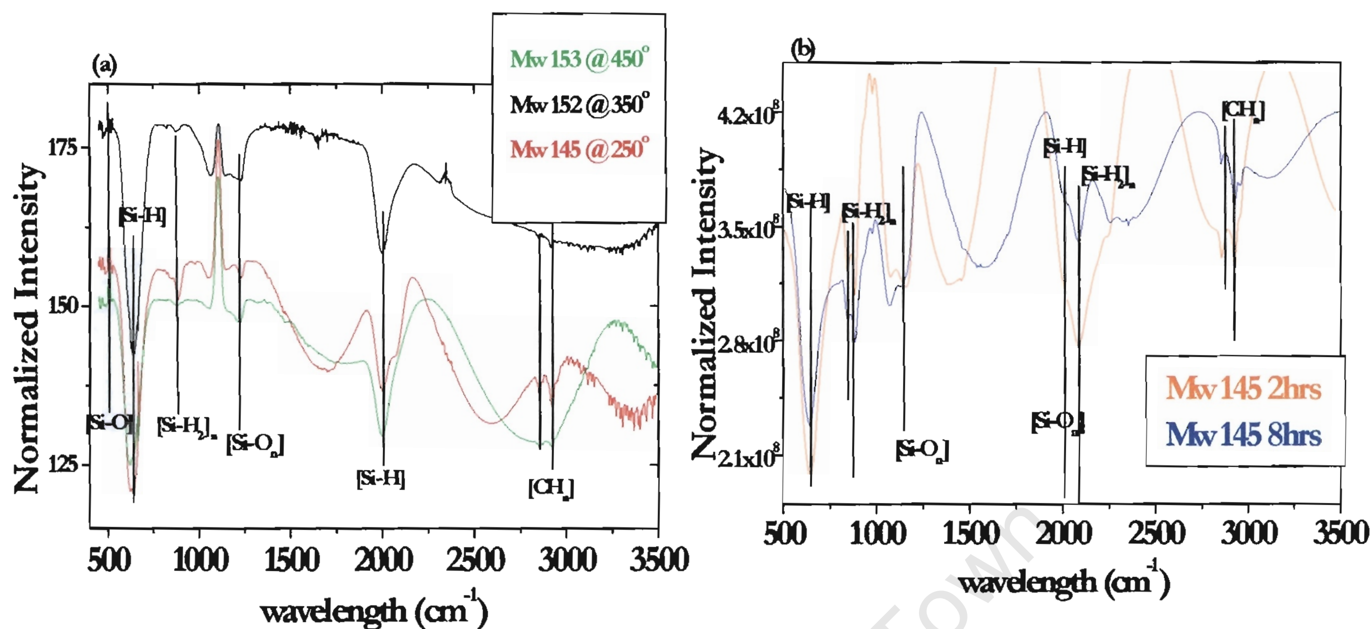

Figure 5.7 (a) The changes in the bonding related to the deposition temperature after 24 hours and, (b) related to illumination time.

Figure 5.7 (a) follows the changes in the bonding structure after 24 hours of illumination, in all the samples the mono-hydrides are now the dominant bonding species (2000 and 640) cm^{-1}, with lower deposited sample Mw 145 (red line) showing a small vibrational mode at 2088 cm^{-1}. The CH_n bond at (2850-3500) cm^{-1} seems not to be affected by illumination. In Figure 5.7 (b) the difference in bonding structure is monitored for sample Mw 145 (Orange line) after 2 and 8 hrs (purple line) and the changes in bonding structure is clearly visible.

University of Cape Town

5.2 X-Ray diffraction.

The direct x-ray diffraction pattern is shown in Figure 5.8 (a), it yield diffuse diffraction peaks characteristic of all amorphous material for all the samples. There is no detectable crystalline contribution from the layer for both the as deposited samples Figure 5.8 (a) and illuminated samples (not shown).

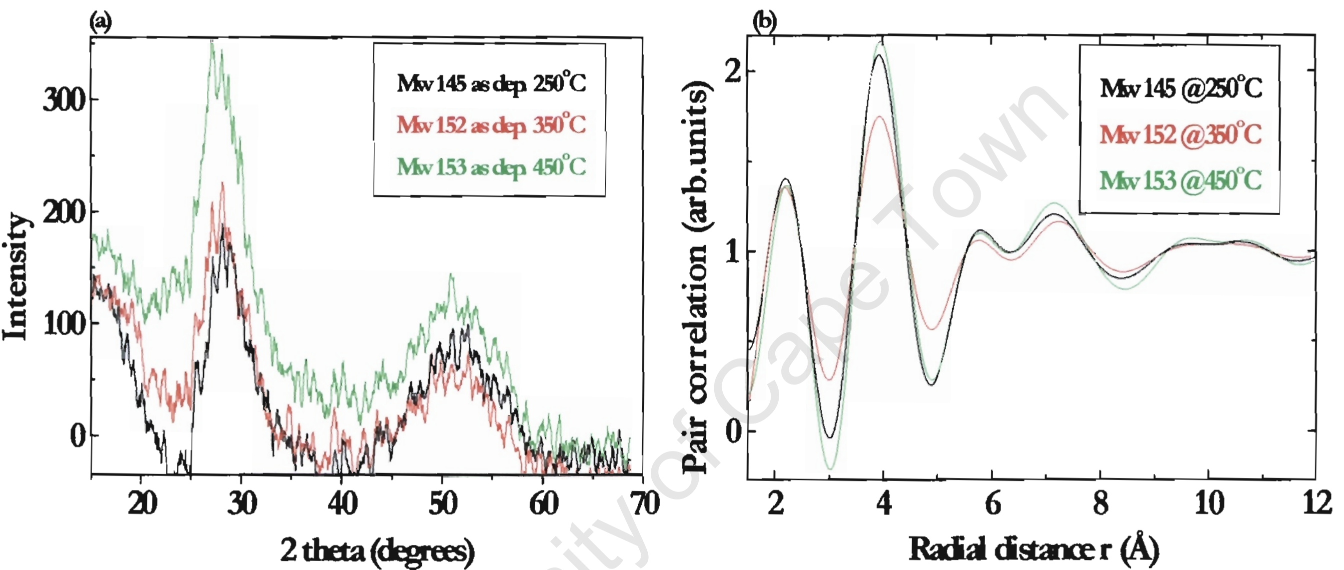

Figure 5.8 (a) The x-ray diffraction results for all the samples, the intensity Vs 2-theta angle. (b) radial distribution function J(r) against the radial distance r, all the major peaks follow the same trend.

Figure 5.8 (b) shows the radial distribution density function (RDF) of the 3 samples studied: They all show a sharp first peak (Si-Si bond length) at small inter-atomic distances r_1. And a broad second peak which is associated with the radial distance r_2 and variation of the bond angle Φ. Both the two peaks are as a result of the presence of short range order (SRO). The absence of the third diffraction peak is associated with absence of the long range order (LRO).

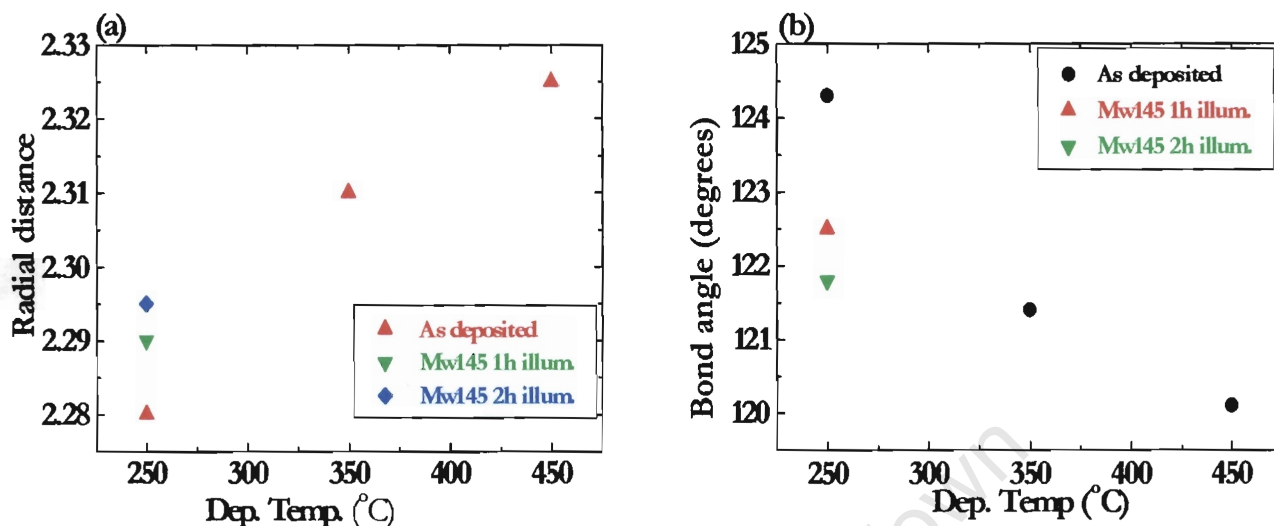

Figure 5.9 (a) The radial distance r as a function of deposition temperature, (b) The variation of the bond angle with the deposition temperature.

University of Cape Town

From Figure 5.9 (a) the radial distance r increases with an increase in deposition temperature (red triangles) and illumination as shown in sample Mw 145 (green and blue symbols). From Figure 5.9 (b) the bond angle for as deposited (black dots) decrease with an increase in deposition temperature. For illuminated samples (red and green triangles) there is a decrease in bond angle with illumination time.

5.3 Scanning Electron Microscopy (SEM).

Figure 5.10 (a) to (d) bellow show the SEM micrographs of sample Mw 145, Mw 150 and Mw 153 deposited 250°, 350° and 450° respectively. The micrographs follows the morphology of the sample due to both the growth temperatures Figures 5.10 (a) and 5.11 (a) and (c) and illumination times, as can be seen from Figures 5.10 (a) and 5.11 (a), (b), (c) and (d) the surface smoothness depends on both deposition temperature and illumination times.

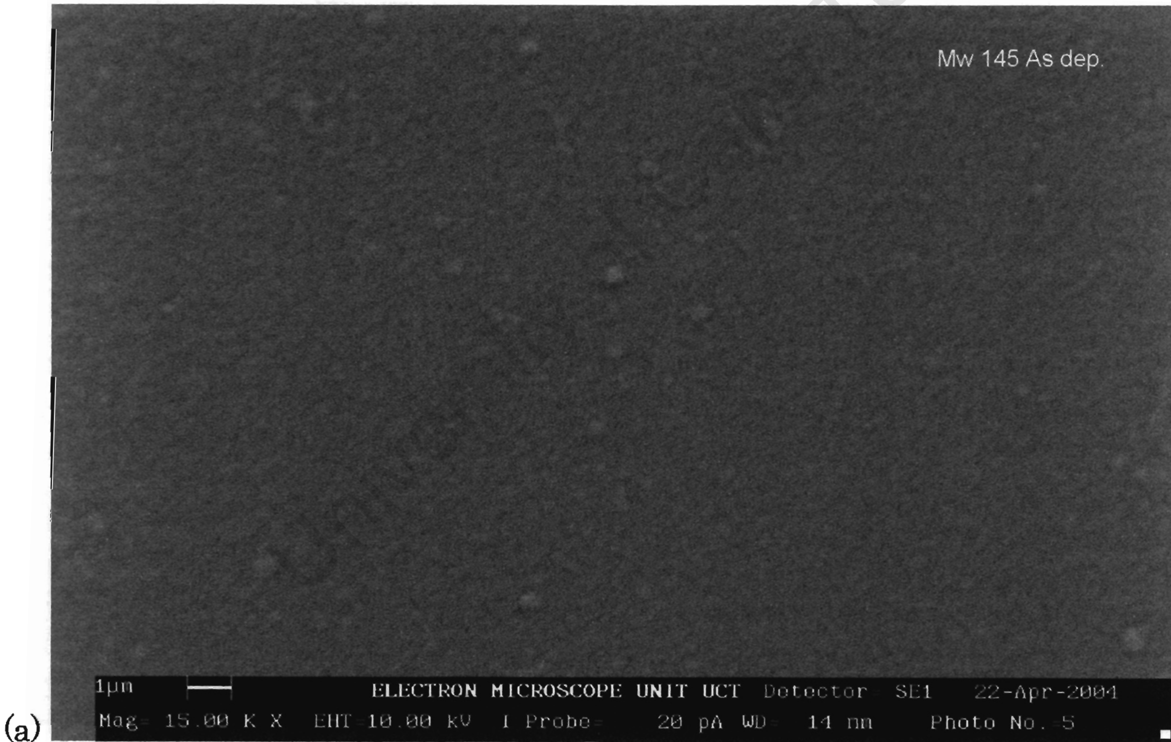

(a)

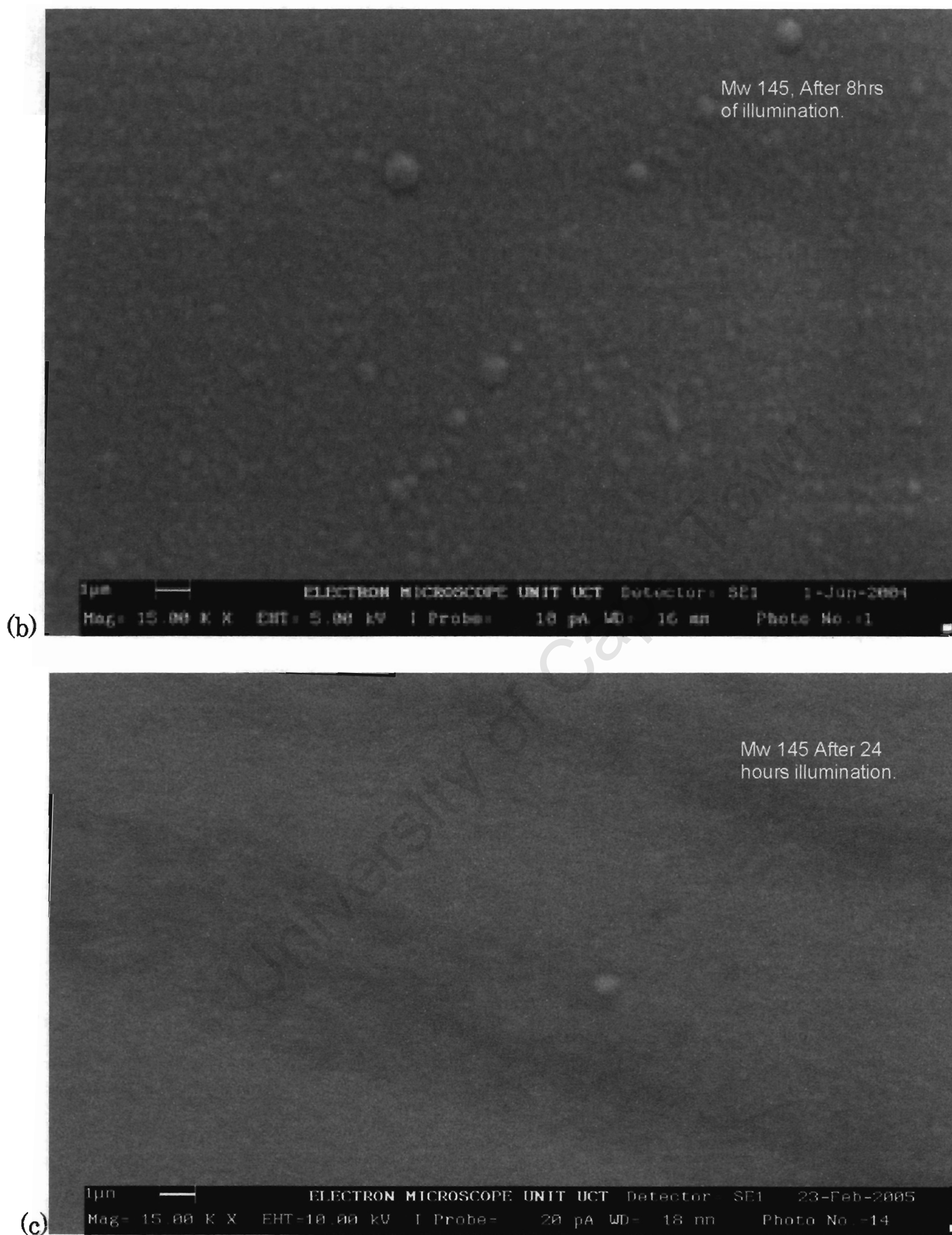

University of Cape Town

Figure 5.10 (a), (b) and (c), shows the SEM micrographs of sample Mw 145 deposited at 250°,as deposited, after 8 and 24 hours of illumination respectively.

(a)

(b)

Figure 5.11 (a) and (b), shows the SEM micrographs of sample Mw 150 deposited at 350°, as deposited and 24 hours of illumination.

(c)

(d)

University of Cape Town

Figure 5.11 (c) and (d) shows samples Mw 153, as deposited and 24 hours of illumination.

5.4 Transmission Electron Microscopy (TEM).

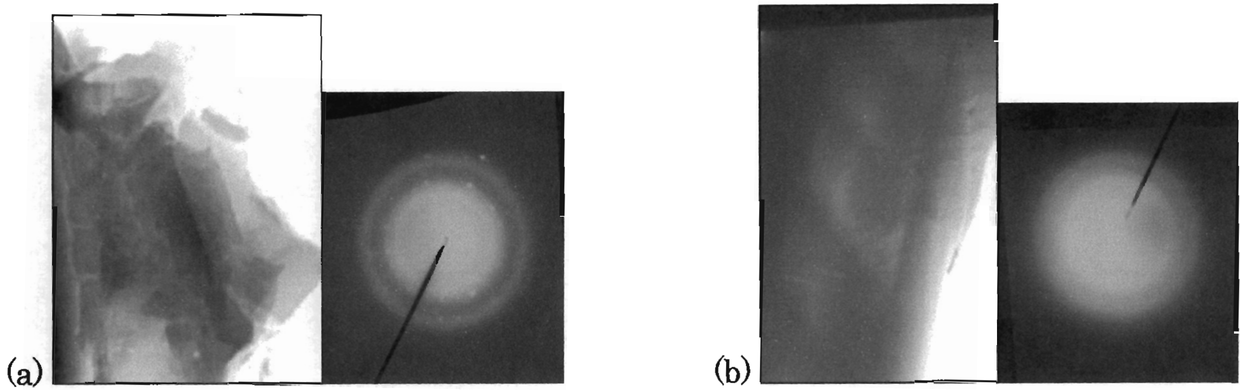

Figure 5.12 TEM and diffraction micrographs of samples (a) Mw 153 deposited at 450° C, (b) Mw 145 deposited at 250° C.

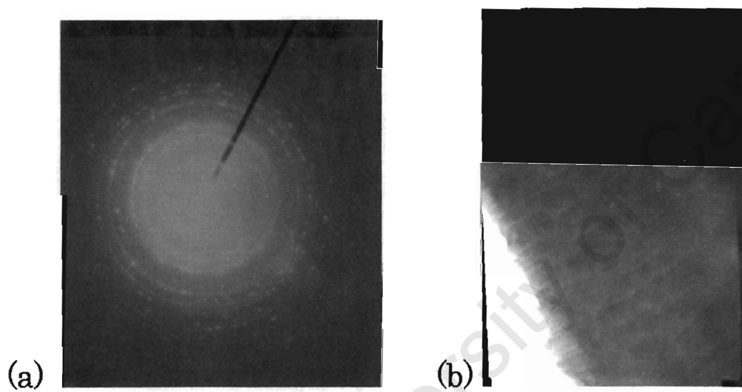

Figure 5.13 (a) Electron diffraction pattern of sample Mw 145 after 24 hours of illumination, (b) TEM micrograph of Mw 145.

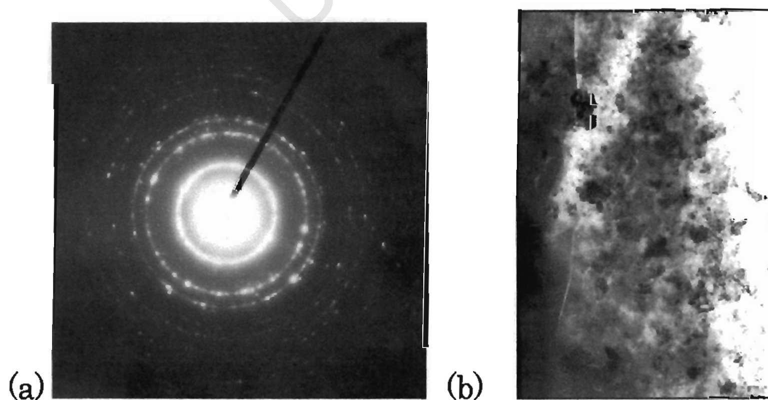

Figure 5.14 (a) Electron diffraction pattern of sample Mw 153, after 24 hours of illumination (b) TEM micrograph of Mw 153 showing crystals.

University of Cape Town

Plane view bright field electron micrograph and electron diffraction pattern of samples deposited at higher and lower temperatures before illumination, Figure 5.12 (a) and (b) respectively. The diffraction patterns are dominated by amorphous rings as can be shown.

The microstructure of the low growth temperature sample after 24 hours of illumination is illustrated in Figure 5.13 (a). Long grains and cracks extending a long way down the sample can clearly be observed. Our medium resolution micrographs do not show if these cracks are voids or are filled with a thin amorphous tissue. The electron diffraction ring pattern shows the presence of poly-crystalline rings embedded structures embedded in amorphous matrix.

For the high growth temperatures Figure 5.14 (a), the micrographs show crystallites embedded in amorphous matrix, this is also confirmed by the electron diffraction results Figures 5.14 (b) which shows that poly-crystalline rings are dominant. On the other hand, only a very faint x-ray signal indicative of crystallinity was observed.

University of Cape Town

6 Discussions.

6.1 Hydrogen, Silicon and Oxygen bonding structures (FTIR spectra).

6.1.1 Hydrogen content.

The knowledge of the hydrogen bonding content and its transport in the a-Si:H matrix is essential for the understanding of its optical and micro-structural properties, moreover the metastability as well as thermal diffusion has been attributed to hydrogen [47, 48].

From the optical transmission (%T) measurements (Figure 5.2 (b)), the film thickness (d), the growth rate, the refractive index (n_o), the optical absorption coefficient (α_{2eV}) and the band gap E_g as functions of photon energy wavelength $h\nu$ were extracted. The thickness and the band gap were both found to decrease with an increase in deposition temperature Figure 5.4 (a) and (b). Whereas the refractive index and absorption coefficient increase with the growth temperatures, table 1 and Figures 5.4 (a) and (b).

The hydrogen concentration as a function of substrate temperature is plotted in Figure 5.3 for both the total hydrogen content (a), molecular and bonded hydrogen content C_H (b). C_H is determined from the (IR) spectra using the integrated absorbance of the wagging–rocking mode at 640 cm^{-1} (Figure 5.7). This vibrational mode's oscillator strength does not depend on the a-Si:H film preparation conditions and on hydrogen content [22]. In all cases hydrogen content follow the same trend *i.e.* decrease from 11.6 to 5.2 % with increasing deposition temperatures and from 10.8 to 5.5 % with illumination times.

University of Cape Town

The hydrogen concentration decrease is attributed to the fact that hydrogen is present as weakly bonded species, in the form of di-hydrides ($Si-H_2$) or poly-hydrides $(Si-H_2)_n$ configuration. This can be seen from the IR spectra band stretch mode at 2100 cm^{-1} and wag mode 889 cm^{-1} which increases with the decrease in both growth temperatures and illumination times Figures 5.6 and 5.7. This effect is well known and can be explained by hydrogen incorporation during deposition [49]. The void rich structure is consistent with the presence only of $(Si-H_2)_n$ chains Figure 5.6, which are known to lower the formation of such structural in-homogeneities.

6.1.2 Molecular Hydrogen H_2.

The difference between bonded and the total hydrogen content is termed molecular hydrogen H_2, and is due to the presence of un-bonded hydrogen in the a-Si:H matrix, possibly located in the structural in-homogeneities such as large size micro-voids or vacancies, and prevalent in low temperature deposited samples (Figures 5.6 and 5.7) [50, 51]. In our samples the molecular hydrogen concentration, is decreasing with the increase in both the deposition temperature *e.g.* for Mw153 sample deposited at 400°C (47%) and Mw152 deposited at 350°C (29%), and illumination time. This can be explained from studies which indicate that, for a-Si:H film deposited at low temperatures, a relatively open void rich structure is deposited, allowing for rapid diffusion of molecular hydrogen at rather low deposition temperatures. This structure is hardly changed by annealing and light soaking [23]. Meanwhile, for higher growth temperatures the film grown is more compact, and

University of Cape Town

hence not permeable to hydrogen molecules. Hence, molecular hydrogen H_2, when incorporated in the film during deposition or annealing/ light soaking will effuse readily at low growth temperatures, while it will be trapped in the material at high growth temperatures.

6.1.3 Hydrogen Bonding Structure.

The thin vertical lines in Figures 5.6 and 5.7 indicate the peak positions of different absorption modes of pure hydrogenated silicon a-Si:H amorphous silicon at (640, 840, 2000 and 2090) cm^{-1}. There is a narrowing of the transmission bands and, at the same time the vibration frequencies of the rocking-wagging modes are shifted to lower frequencies, which indicates a clear change in bonding nature and in bonding environment, from (644 to 625) cm^{-1}, brought about by the increase in deposition temperature and a shift from (641 cm^{-1} to 634 cm^{-1}) brought about by an increase illumination times.

All the samples have similar bending bands, with two well separated components centred around (840-894) cm^{-1} respectively. These bands are hardly detected for the samples with high deposition temperatures Figure 5.6 (a), and are associated with weakly bonded species *i.e* di-hydrides ($Si\text{-}H_2$), or poly-hydrides $(Si\text{-}H_2)_n$ (isolated or clustered) [52]. As expected their intensity decrease with the increase in deposition temperature and illumination time. This is in total agreement with the literature, which suggest that these features are associated with device

University of Cape Town

quality a-Si:H as they tend to shifts (dissociate) towards the more stable mono-hydrides (Si-H) [53, 54].

There is a double peak centered around the (2000- 2100) cm^{-1} vibrational modes for samples deposited at low temperatures, the 2100 cm^{-1} is associated with the stretching modes of vibration of the poly-hydrides $(Si\text{-}H_2)_n$, di-hydrides $(Si\text{-}H_2)$ or clustered mono-hydrides $(Si\text{-}H_n)$ [53, 55]. Again this peak is not observed for samples deposited at high temperatures. The only peak present is centered on 2000 cm^{-1} and is associated with mono-hydrides (Si-H) [49, 54] and it seems to also increase with deposition time and illumination time Figure 5.6 (a), (b) and 5.7 (a), (b). For the low temperature deposited samples, there is a shift of the IR peak at 2100 cm^{-1} shift to 2088 cm^{-1} with its intensity decreasing with deposition temperature (Figure 5.6 (a)), which suggests that those hydrogen atoms in a di-hydride configuration are unstable at high temperatures.

With light soaking (Figure 5.6 (b)) this peak shift continues, and after 24 hours this peak is now the dominant peak (Figure 5.7 (b)). The increase in hydrogen content C_H and peak intensities with the decrease in growth temperature and illumination time has been attributed to the increase in silicon di-hydride at this peak 2100 cm^{-1} [49]. As the deposition temperature and illumination time is increased the hydrogen of the weakly bonded species start diffusing due to the dissociation of the weak bonds and lead to the decrease intensity around these bonds. It has been established that the hydrogen realized by the dissociation of these poly-hydride groups can readily

University of Cape Town

diffuse out of the sample, and that the sample deposited at high growth temperatures with less poly-hydrides corresponds to a rather dense a-Si:H material containing spherical voids [55, 56]. In this case, a fraction of hydrogen realized at low temperature, from the dissociation of poly-hydride groups can be trapped in these cavities and possibly passivate dangling bonds at their internal surface [57].

All these vibration modes *i.e.* rocking-wagging, bending and stretching modes around 2100 cm^{-1} can clearly be assigned to the di-hydride bonds on (100) and (111) surface in silicon crystallites. Therefore we conclude that, for high substrate temperatures and longer light soaking, apart from a certain amount of amorphous phase still present, formation of microcrystalline silicon occurs and hydrogen is preferentially bonded at the surface of the microcrystalline grains, this is confirmed by our electron diffraction results (Figure 5.13).

The integrated intensity of the IR mode at (2850 to 3050) cm^{-1} is attributed to the stretching vibrations of the CH_n group in both sp^3 and sp^2 configurations [59]. The IR integrated intensities of SiH_n and CH_n groups decrease with the increasing deposition temperature illumination time, which suggests that hydrogen effusion occurs. Carbon incorporated into a-Si:H, will lead to the new defect induced by carbon entering into the network and the formation of the CH_n configurations [56].

University of Cape Town

6.1.4 Oxygen Bonding Structure.

As H diffuses it leaves gaps through which oxygen that resides on the film, diffuse or move into the film, either as Si-O-Si or as Si-O as shown by the IR spectra Figures 5.6 to 5.8, where we observe the oxygen vibrational modes Si-O_n at (1100-1200) cm^{-1}. In the same vibrational mode region, we have an emission peak centred at 1105 cm^{-1}. All these oxygen vibrational modes interestingly enough are not observed for as deposited samples, they start to appear after 2 hrs of illumination. As in the Si-H vibrational modes the oxygen vibrational peaks intensities shifts to the lower wave numbers and they also seems to increase with growth temperature and with illumination time Figures 5.6 to 5.8. After 24 hours we observed a small peak centred around (514 -501) cm^{-1} which is attributed to Si-O group normally centred around 500 cm^{-1} (Figures 5.6 (b) and 5.7).

With RBS, the resonance scattering at the energy 3.05 MeV is supposed to give a high yield of oxygen on the sample deposited at a lower growth temperature, which signifies the presence of oxygen as an impurity in the Si-network. The value of the impurities amount to 5.0 at % as a result of non compact nature of the sample grown at lower temperature, whereas in our samples the O was only detected in one sample and the oxygen concentration was very low 1%. This is expected since the only source of this oxygen could be oxidation or contamination during deposition, which in our case was negligible, as we were careful in handling our samples during deposition [58]. Illumination did not have any effect on the oxygen content.

University of Cape Town

6.1.5 Band Gap.

The optical absorption spectra were used to obtain the band-gap E_g, using the Tauc relationship in the high absorption region ($\alpha \sim 10^4$ cm^{-1}) [61]. Figure 5.2 (a) shows a Tauc plot (plot of $(E)^{1/2}$ versus E), extrapolated to zero absorption in our samples. The band-gap E_g varied within (1.82 -1.70) eV range, which is the range for the device quality a-Si:H Table 1 and Figure 5.2 (a). The optical band gap E_g increased linearly with increasing hydrogen content C_H (Figure 5.5 (a)) and decreased with the increase in deposition temperature and absorption coefficient (α_{2ev}) (figures 5.6 (a) and (b)) as expected.

The energy band gap E_g decrease is attributed to an increase in bond angle Φ as the temperature is decrease, which will then lead to the degradation of optoelectronic properties of the film accompanied by the increase in defect density [62]. It has been shown that as hydrogen content increases, the distance between Si atoms increases slightly in this regime, as the band gap E_g correlates with the silicon inter-atomic distance [8].

With illumination the band gap E_g remains constant, this was expected as Feenstra [63] showed that, for hot-wire deposited samples, even for hydrogen concentrations as low as 1 at %, the Tauc band gap remains as high as 1.7 eV [64]. This effect was attributed to the presence of micro-voids in the material, which left the Si-Si bond density constant in the most-dense phase, as in HWCVD the additional of hydrogen atoms are not incorporated in isolated Si-H bonds. Rather $(Si\text{-}H)_2$ chains and voids are formed, which have no effect on the Si-Si bond constant in the density

University of Cape Town

in the dense phase. As the optical band gap is determined by the phase with the smaller band gap, the band gap is constant in this region [64].

6.2 Scanning Electron Microscopy (SEM).

The scanning electron micrographs of the samples are shown in Figure 5.10 and Figure 5.11, which reveals a granular (flaky with bubbles 2µm diameter) structure which tends to become fine and compact as the deposition temperature increases. This feature is confirmed by results in table 1, where the absorption coefficient (α_{2ev}) increases from (1.33 to 2.88) x10^4 cm^{-1}, with the increase in deposition temperature, indicating that a compact material is deposited at higher temperatures. This can also be explained by the surface mobility of the precursors, which is strongly dependent on the substrate temperature [65].

Figure 5.10 shows sample Mw145 deposited at 250°C, for as deposited (a) and after 8 hours (b). The film is becoming rougher, but at this point, most of the hydrogen atoms are still weakly bonded to the silicon as poly, di-hydride species, and hydrogen diffusion is still at its peak. As noted by Winer and Street [66] that hydrogen atoms are more mobile than Si atoms in a a-S:H, this motion allows the inter-conversion of the defects weak bonds and strong bonds. They proposed that those processes occur at subsurface growth zone [66].

After 16 hours the samples start to smoothen, this might be caused by the fact that hydrogen at this point will diffuse at a slower rate, since most of the weakly bonded species are now dissociating and hydrogen is strongly bonded to Si to form a

University of Cape Town

more stable Si:H, and this is accompanied by the hydrogen content C_H which is becoming more stable see Table 1.

After 24 hours of illumination the morphology becomes smoother as most of the bonds in film are Si-H bonds Figure 5.10 (c), and there are also some defects seen on top surface, these defects might be from the substrate. This behaviour can also be observed for samples Mw 150 and mw 153 Figure 5.11 (a) to (d). This can be explain in the following manner; as the hydrogen diffuse it terminates most of the dangling bonds and leaves behind strong Si-H bonds, samples become smoother, and the defects from the substrate can be easily seen.

6.3 Transmission Electron Microscopy (TEM).

TEM micrographs of as grown samples are shown in Figures 5.12 (a) and (b). For lower growth temperatures, the thicker film shows a smooth amorphous surface with no evidence of crystals while for the higher growth temperatures, we observed cracking of the film which seems to indicate the formation of nano-crystallites embedded in an amorphous phase (Figure 5.14 (a)). This is confirmed by the electron diffraction patterns which indicate that at this stage our samples are amorphous (Figure 5.12).

After 24 hours of illumination the diffraction pattern of the samples showed definite poly-crystalline rings structures which decrease with deposition time as seen in Figures 5.13 and 5.14. This suggest that poly-crystalline rings are embedded in the amorphous network as seen from Figures 5.13 and 5.14, this is in agreement with all

University of Cape Town

of our results from hydrogen bonding, molecular hydrogen, SEM, RDF and the energy band gap E_g results.

All the above results are also in agreement with theory and experiments, which states that total crystallization depends on the growth temperature of the a-Si-H [68]. Hence we can conclude that the sample have an absorption curve between that of μc-Si:H and a-Si:H [72, 73]. On the other hand, only a very faint x-ray signal indicative of crystallinity was observed in Figure 5.6 (a).

The total crystallization time falls linearly with illumination time, as the growth temperature increases from (250 to 450)°C Figures 5.12 to 5.14, this correlates well with the total hydrogen content of the film, which groups linearly from (11.6 to 4.2) % as the growth temperature and illumination time is increased. Thus the corresponding material is homogeneously structured, within this range for low temperatures deposited samples, Table 1 and most of hydrogen is present only in Si-H bonds, and there are fewer voids in the material Figure 5.8 [69].

6.4 X-ray diffraction.

The direct x-ray diffraction patterns from the samples studied yields diffuse diffraction peaks characteristic of all amorphous material Figure 5.8 (a). There is no detectable nano-crystalline contribution from the layer for both the as deposited and illuminated samples. Information about the local order in a-Si:H layer comes from the radial distribution function obtained from x-ray scattering.

University of Cape Town

Figure 5.8 (b) shows the radial distribution density function (RDF) of the 3 samples studied: They all show a sharp structure at small interatomic distances. This can be associated to the changes at a short-range scale, which are associated to the changes in the 1st and 2nd peak positions and shapes with increasing deposition temperature. The first peak in the radial density function arising from the nearest neighbour atoms giving us average Si-Si bond length r_1 whereas, the 2nd peak arising from the 2nd nearest neighbour atoms at a distance r_2 and the bond angle Φ. The width of the 2nd peak is also changing and that is an indication of the change in the bond angle and all are related to the presence of the short range order (SRO). As expected, we observe the diffusing of the third peak associated with the absence of long range order (LRO).

Qualitative estimates for the bond angle and the bond length taken from the peak position are plotted in Figures 5.9 (a) and (b). There is a slight increase in the bond length and a decrease in the bond angle associated with an increase in deposition temperature indicating a continual relaxation of the amorphous network. The bond angle decreases from 122° to 119° while the bond length increased from 2.28 to 2.33 Å.

University of Cape Town

7. Conclusions

The optoelectronic properties of the film deteriorated gradually with the decrease of optical band gap E_g, which is normally accompanied by the increase in defect density. Hence the quality of the film increases with deposition temperatures since the low band gap is accompanied by the reduction of bonded hydrogen and the increase of the compactness of the film.

It has been established that for amorphous silicon made at lower substrate temperature using tantalum filaments, the hydrogen concentration lies between 8 at % and 15 at %. As a result, the corresponding Tauc band gap remains high, with values between 1.75 eV and 1.86 eV [3]. This correlates exactly with our results as the hydrogen content lies within this range for low temperature deposited samples, table 1 and the band gap was high (1.82 eV) for all the samples.

The increase in the density of the Si-H bonds as a result of the light illumination strongly suggest the optically induce formation of Si-H bonds as a plausible mechanism for the observed light induced annealing effect in our samples. This corroborates with experimental work done on electron spin resonance (ESR) performed by Zhang et al [70] and Takeda et al [71] on undoped a-Si:H subjected to photo illumination. Hence we can conclude that, when our a-Si-H samples were illuminated by light:

a) Light – induced annealing of dangling bonds occurs, especially the ones located around the voids, which suppress the photo-creation of defects around the

University of Cape Town

voids. The numbers of weak Si-Si bonds adjacent to the Si-H bonds are reduced compare to the bulk due to relaxation of the network around the voids.

b) Light – induced creation and annealing of dangling bonds in the bulk, occurs.

University of Cape Town

References.

[1] H. Wiesmann, A.K Gosh, T. McMohan, M. Strongin, J. Appl. Phys. Vol. 50 (1979) 3752.

[2] Physics of Amorphous Semiconductors, Kazuo Morigaki, (1999) Imperial College Press (chapter 3 p23).

[3] A.H Mahan, J. Carapella, B.P Nelson, R.S. Crandall, J. Appl. Phys. Vol. 69 (1991) 6728

[4] S. Bauer, B. Schroeder, W. Herbst, M. Lill. Proc. 2nd. World Conf. on Photovoltaic. Solar Energy Conversion, 363 (1998).

[5] S.R Elliott, Physics of amorphous materials, 2nd edition, Longman, UK, (1990).

[6] H. Nomura, K. Akimoto, A. Kono, T. Goto, J. Appl. Phys. D: Appl. Phys 28, (1995).

[7] A. Madan and M.P Shaw, Physics and applications of amorphous semiconductors, Academic Press, San Diego, 1988.

[8] R.A Street, Hydrogenated Amorphous silicon, Cambridge solid state sciences Series.Cambridge, (1991).

[9] D.L Steabler and C.R Wronski, App. Phys. Lett. 31, 292 (1977).

[10] T. Tsu and P.C Taylor, Phy. Rev. Lett. 89 (2000) 015502.

[11] M.H Branz, Solid State Commun.105 (1997) 387.

[12] W.H Zachariasen, J. Am. Chem. Soc. 54 (1932) 3841.

[13] H.P Klug and L.E. Alexander, X-ray diffraction procedures for polycrystalline and amorphous materials, 2nd edition, (1978).

[14] P.M Voyles, J.R Abelson, Medium-Range Order in Amorphous Silicon measured

University of Cape Town

by fluctuation Electron Microscopy. Final Report 23 june 1999- 23 August, University of Illinois at Urbana- champaign Urbana, Illinois (page 10 -11).

[15] M. Stutzmann, W.B Jackson. C.C Tsai, Phys. Rev. B 32 (1985) 23

[16] T. Dietrich, S. Chiussi, M. Marek, A. Roth, and F. Comes, J. Appl. Phys. Chem. 95, 9302 (1991).

[17] C. Godet, P. Roca, I. Cabarrocas, J. Appl. Physics. 80 (1996) 97.

[18] D.E Carlson, J. Vac. Sci. Technol. 20290 (1982).

[19] F. Stillinger, T. Weber, Phys. Rev. B 31, 5262 (1985).

[20] Wooten, K. Winer and D. Wier, Phys. Rev. Lett. 54, 1392-1395 (1985).

[21] E. Kim, and Y.H Lee, Phys. Rev. B 49, 1743 (1994).

[22] E. Kim, and Y.H Lee, Phys. Rev. B 50, 18084 (1994).

[23] J.M Holender, G.J Morgan. J. Appl. Phys: Condensed. Matter. 4 (1992) 4473.

[24] Biswas, C.Z Wang, C.T Chan, K.M Ho, C.M Soukoulis, Phys. Rev. Lett. 63, 1491 (1989).

[25] J.M Holender, G.J Morgan. J. Appl. Phys: Condense Matter. 3 (1991) 1947.

[26] F.A Fedders, Y. Fu, D.A Brabold, Phys. Rev. B 68, 1888 (1992).

[27] A.E Delahoy, and R.W Griffith. Conf. Rec. IEEE Photovoltaic Spec. Conf. 15, 704 (1981).

[28] R.S Grandall, D.E Carlson, A. Catalano, and H.A Weakliem, Appl. Phys. Lett. 44, 200 (1984).

[29] M. Stutzmann, W.B Jackson, C.C Tsai. Appl. Phys. Lett. 45,1075 (1984)

University of Cape Town

[30] G. Lucovsky, J. Yang, S.S Chao, J.E Tyler and W. Czuba-Tyj. Phys. Rev. B 28, 3225 (1983).

[31] A. Frazer, Vibrational lifetime of Interstitial Oxygen in Crystalline Silicon. Phd Thesis, Dept. Phys. The College of William and Mary (2002).

[32] J. Jasinski, B. Meyerson, and B. Scott, Ann. Rev. Phys. Chem. 38 (1987).

[33] H. Dersch, J. Stuke and J. Beichler, Appl. Phys. Lett. 38 (1980) 456.

[34] W. Kaizer, P.H Keck and C.F Lange, Phys. Rev. 101, 1264 (1956).

[35] R. Deshpande, S. Kothari, A. Dillon, H. Mahan, J. Allen, Z. Zhang and S. Mitra, 3rd International conference on (HWCVD), Utrecht University (2004).

[36] J. Doyle, R. Robertson, G. Lin, M. He, and A. Gallagher, J. Appl. Phys. 64, 3215-3223 (1988).

[37] P. Skell and P. Owen, J. Am. Chem. Soc. 1972, 94, 5434 .

[38] P. Gasper, B. Boo, D. Svoboda, J. Appl. Phys. Chem. 91, 5011 (1987).

[39] K. Tanaka, A. Matsuda, Mater. Sci. Rep, 2 (1987) 139.

[40] C. J. Fang, K.J Grutze, L. Ley, and M. Cardona, J. non-Cryst. Solids, 35-36 (1980) 255.

[41] J.C Knight, Jpn. J. Appl. Phys. 18 (1979) Supp. l, 101

[42] G.E Jellison Jr, F.A Modine, App. Phys. Lett. 69 (1996) 371.

[43] D.B Williams, C. B Carter, Transmission Electron Microscopy I (1996) Plenum Press, New York.

[44] D.T Britton, M. Härting, Z. Sigcau and E. Minani, Thin Solid film. Vol.430, (2003) 149-152.

University of Cape Town

[45] H. S Povolny and X. Deng. Thin Solid Film.Vol. 430, (2003) 125-129.

[46] U. Kroll, J. Meier, P. Torres, J. Pohl, A. Shah, J. Appl. Phys. 80 (1996) 497

[47] W. B Jackson, J.M Marshall, M.D Moyer. Phys. Rev. B 39, 1164 (1989).

[48] W. B Jackson, T. Tsai. Phys. Rev. B 45, 6564 (1992).

[49] M. H Brodsky, M. Cardona, and J.J. Cuomo. Phys. Rev. B 19, 3556 (1979).

[50] P. Danesh, B. Pantchev, K. Antonova, E. Liarokapis, B. Schmidt, D. Grambole J. Baran, J. Appl. Phys, D. 37, 249-254 (2004).

[51] U. Kroll, J. Meier, A. Shah, S. Mikhailov, J. Weber. J. Appl. Phys. 80, 4971 (1986).

[52] C.C Tsai and H. Fritzsche, Sol. Energy Mater. 1, 29 1979.

[53] G. Lucovsky, R. J Nemanich, J.C. Knights, Phys. Rev. B 19, 2064 (1979).

[54] G. Lucovsky, Solar Cells 2 (1980) 431.

[55] J.C. Knights, G. Lucovsky, R.J. Nemanich, J. Non-Cryst. Solids 32 (1979) 393.

[56] H. Mahan, Y. Chen, D.L. Williamson, G.D. Moeney, J. Non-Cryst. Solids 137–138 (1991) 65.

[57] Y. Wu, J.T. Stephen, D.X. Han, J.M. Rutler, R.S. Crandle, A.H. Mahan, Phys. Rev. Lett. 77 (1996) 2049.

[58] A. S. Ferlauto, G. M. Ferreira, J. M. Pearce, C. R. Wronski, R. W. Collins, X. Deng, G. Ganguly, Thin Solid Films, Vol. 455-456 (2004), 388-392.

[59] J. C. Angus, J. E. Stultz, P. J. Shiller, J. R. MacDonald, M. J. Mirtich, S. Domitz, Thin films, Vol. 118 , 311 (1984).

[60] J.Tauc, R. Grigorovici, A. Vancu, Phys. Stat. Sol., 15, p. 627 1966.

University of Cape Town

[61] G.D Cody, C.R Wronski, B. Abrles, R.B Stephans, B. Brooks, Solar Cells 2 (1980).

[62] Y. Bouizem, A. Belfedel, J.D Sib, A Kebeb and L. Chahed, J. Appl. Phys. Condense Matter. 17 (2005) 5157-5158.

[63] K. F Feenstra, R.E.I Schropp, W.F Van der Weg, J. Appl. Phys. 85/9 (1999) 6843.

[64] S.R Jadkar, J.V Sali, S.T. K Shirsagar, M.G Takwale, Solar Energy Material & Solar Cells. 85 (2005) 301-312.

[65] H. Seitz, S. Bauer, R. O. Dusane and B. Schröder. Thin Solid Films, Vol. 395, (116-120) (2001).

[66] R. A Street, K. Winer. J. Non-Cryst. Solids 114, 645 (1989).

[68] K. Pangal, J.C Sturm, S. Wagner, J. Appl. Phys, Vol 85 (1900-1903) (1999).

[69] W. Beyer, H. Wagner. J. Non-Cryst Solids Vol 59-60, (161-168) (1983).

[70] H. Shanks, C.J Fang, L. Ley, M. Cardona, F.J Demond, S. Kalbitzer, Phys. Status Solidi B 43, 110 (1980).

[71] H. Hikita, Y. Kimura, K. Tadeka H. Yokomichi and K. Morigaki J. Non-Cryst. Solids, Vol. 164-166, (1993), 219-222.

[72] U. Kroll, J. Meier, P. Torres, J. Pohl, A. Shah, J. Non- Cryst. Solids 69 (1998) 227.

[73] U. Kroll, J. Meier, P. Torres, J. Pohl, A. Shah, J. Appl. Phys. 80 (1996) 497

[74] G. Tan, P. Zhang, Q. Zhu, S. Peng. J. Non-Cryst. Solids, Vol. 59-60, (417-420) 1983.

[75] R. Swanepoel, priv. comm.2004

University of Cape Town

University of Cape Town